An apparatus for studying interactions between Rydberg atoms and metal surfaces

by

Jeffrey David Carter

A thesis
presented to the University of Waterloo
in fulfillment of the
thesis requirement for the degree of
Master of Science
in
Physics

Waterloo, Ontario, Canada, 2007

Author's Declaration

I hereby declare that I am the sole author of this thesis. This is a true copy of the thesis, including any required final revisions, as accepted by my examiners.

I understand that my thesis may be made electronically available to the public.

Jeffrey David Carter

Abstract

A system suitable for studying interactions between ^{87}Rb Rydberg atoms and metal surfaces has been constructed. This thesis describes the design and construction of the apparatus, and some test results. Atoms in a vapor cell magneto-optical trap are transferred to a macroscopic Ioffe-Pritchard trap, where they will be RF evaporatively cooled and loaded into a magnetic microtrap (atom chip). Confinement of cold clouds at controllable distances (5–200 μm) from a metal surface is possible. The effects of atom-surface interactions can be studied with Rydberg atom spectroscopy.

Some functionality of the apparatus has been demonstrated. Approximately 1.5×10^7 atoms were loaded into a mirror MOT, and about 6×10^6 atoms were optically pumped to the $|F = 2, m_F = 2>$ hyperfine ground state and confined in a macroscopic Ioffe-Pritchard trap. The temperature of the cloud in the trap was 42 ± 5 μK, and the $1/e$ lifetime is 1–1.5 s. Forced RF evaporation has been used to measure the magnetic field at the trap minimum, but RF evaporative cooling has not yet been demonstrated.

Acknowledgements

I would first like to thank my supervisor, Dr. James Martin, for his hard work, dedication, and assistance through this project, particularly in reading through this thesis and making suggestions for revision. Jim's devotion to excellence in research and teaching is an inspiration.

Thanks to Owen Cherry, my M.Sc. colleague on this project. Owen fabricated the atom chips described in this work, assisted in the assembly of the UHV chamber and MOT optics, and took the photographs used in many of the figures in this thesis. Owen was also a valuable source of suggestions and commiseration during my writing.

Thanks to my examining committee, Dr. Wing-Ki Liu and Dr. Gregor Weihs, for their careful reading and suggestions. Thanks also to my advisory committee, Dr. Donna Strickland and Dr. Gregor Weihs, for their time and advice.

Thanks to Maria Fedorov, Joe Petrus, Joel Keller, and Rodger Mantifel for their work in constructing the lab and apparatus. The graduate students in the other Martin lab, Kourosh Afrousheh and Parisa Bohlouli Zanjani, were also very helpful. Blair Lebert, Mukto Akash, and Ian Burgess are currently working on enhancements to the existing experimental setup. I would also like to thank the staff at Science Technical Services, particularly Andy Colclough and Krunomir Dvorski, for their assistance. Thanks also to any people I've inadvertently left out—it's beginning to be a rather lengthy list!

Many thanks to all the friends and family who have encouraged and supported me over the years. Finally, and most importantly, I thank my dear fiancée, Giselle, who has worked very hard at planning our wedding (less than two weeks away as I write this) while I have been caught up in writing, defending, and revising this thesis over the last two months.

Dedication

To Giselle, my Sweet,

for all your love, support, and inspiration.

Contents

List of Tables

List of Figures

Chapter 1

Introduction

1.1 Rydberg atoms

A Rydberg atom is a neutrally charged atom in which one valence electron has been excited to a very high principal quantum number n. The atom can be reasonably described as a loosely bound electron orbiting a positively charged ionic core. As a result, the atomic structure is very similar to hydrogen. An excellent reference book has been written by Gallagher [1] and a few of the most relevant properties of Rydberg atoms will be repeated here.

Many atomic properties scale as powers of n. The excited state lifetime (for low-angular momentum states) scales as n^3. The radiative lifetime of Rydberg states can reach hundreds of μs (ionization and stimulated transitions to other Rydberg states due to blackbody radiation from the walls of a room-temperature vacuum chamber can make the lifetime less in practice). The electric polarizability scales as n^7, so Rydberg atom spectroscopy can be used to detect very small electric fields. Since the spacing between energy levels scales as $1/n^3$, narrow-linewidth excitation sources must be used to avoid exciting multiple states. In the Martin group we routinely excite rubidium atoms (the valence electron is at $n = 5$) to Rydberg states close to

$n = 50$. Thus some atomic properties can be enhanced by orders of magnitude by excitation to Rydberg states.

1.2 Rydberg atom-surface interactions

If a Rydberg atom is near a metal surface, the surface charge of the metal will arrange to form an image of the fluctuating electric dipole moment of the atom. The dipole-dipole interaction between the atom and its image will create an attractive potential. In the near field, the potential has a $1/r^3$ distance dependence and is known as the Lennard-Jones potential [2]. This effect has been observed by passing a beam of sodium atoms excited to Rydberg states between two metal-coated glass slides separated by a few μm and measuring the number of transmitted atoms [3]. In the far field, retardation effects must be taken into account. The potential in the far field has a $1/r^4$ scaling with distance and is called the Casimir-Polder potential [4]. A good review of perturbative atom-surface interactions has been written by Hinds [5].

Other atom-surface interactions are possible. As a Rydberg atom gets close to a metal surface, the electron is attracted to its image and can escape to the surface, ionizing the atom. Field ionization of Rydberg atoms in a sodium atomic beam passed through a μm-scale mesh has been observed experimentally. This method was used to measure the physical size of Rydberg atoms [6].

Other interesting Rydberg atom-surface interaction experiments have been performed by firing beams of potassium [7] or metastable xenon [8], [9], [10] at single-crystal metal or semiconductor surfaces at grazing incidence. The atoms are field ionized as they come close to the surface, and the ions are swept to a charged-particle detector by an electric field. The atomic motion can make interpretation of the results rather complicated, as atoms tend to undergo avoided crossings and change states as they fly toward the surface [9]. Additionally, detection of the atoms is only possible

in a relatively strong electric field, which tends to mix different Rydberg states.

Near surfaces, spatially inhomogeneous electric fields or *patch potentials* are present due to inhomogeneous distribution of the surface charge. This may be due to contamination of the surface and/or the random orientation of the polycrystalline grain structure of most metal surfaces. The effects of patch potentials due to adsorbates have been seen in experiments where alkali metals were deposited on surfaces [11], [7]. The concentration of adsorbed atoms tends to change with time and can make repeatable experiments in such an environment difficult. Time-varying patch potentials are also suspected to be responsible for the anomalous heating observed in microfabricated ion traps [12], [13]. Further experimental studies of the nature of these patch potentials will be helpful in reducing their effect.

1.3 Ultracold atoms

At short atom-surface distances, atom-surface interactions can be conveniently studied using cold atoms trapped near the surface. The cooling and trapping techniques required are well developed and frequently used in experiments with quantum degenerate gases. Several experiments have employed Bose-Einstein condensates (BECs) to study atom-surface interactions. Electric fields due to rubidium adsorbates on surfaces have been measured by observing changes in the mechanical oscillation frequency of a nearby BEC [14]. The same technique has also been used to measure the $1/r^4$ attractive Casimir-Polder potential [15]. The Casimir-Polder potential for dielectric surfaces has also been measured by observing the distance dependence of the lifetime of a BEC confined near a dielectric surface [16].

Recently developed magnetic microtraps can trap atoms with magnetic fields generated by μm-scale current-carrying wires [17], [18]. Cold clouds of atoms to load these traps can be generated with vapor-cell magneto-optical traps [19] and RF evaporative

cooling [20]. Cold atoms confined in a magnetic microtraps can be excited to Rydberg states at a known, controllable distance from surfaces, without the complications of atomic motion or large electric fields encountered in previous experiments.

1.4 Outline

This thesis details the progress to date in the construction of an apparatus suitable for studying Rydberg atom-surface interactions. There are five chapters, including this introduction.

Chapter 2 provides a theoretical overview of some of the techniques used in this experiment. Particular attention is given to magnetic trapping, including magnetic microtraps or "atom chips". This chapter also describes magneto-optical trapping, RF evaporative cooling, and measurement of the temperature of cold atomic clouds using ballistic expansion.

Chapter 3 describes the design and construction of the experimental setup. This includes the design, construction, and performance of the ultrahigh vacuum system. Design and performance of the devices for magnetic field generation (coils, macroscopic current-carrying structures, and the atom chip) are included. The laser systems used for the MOT and imaging are described, as well as the imaging system and procedure. Finally, the RF evaporative cooling scheme and the control system are discussed.

Chapter 4 consists of experimental results. The experimental sequence is given in detail. The performance of the MOT and the first stage of purely magnetic trapping are characterized. Finally, some characterization of the trap using RF evaporation is shown.

Chapter 5 contains a summary of the results, an outline of future work, and some recommendations to consider on future implementations of this design.

Chapter 2

Theory

2.1 Introduction

This chapter provides a theoretical overview of some of the techniques used in this experiment. Magnetic trapping of paramagnetic atoms is described. Magnetic atom guides and traps created with current-carrying wires and homogeneous magnetic fields are discussed. The use of magnetic microtraps, consisting of μm-scale wires fabricated on substrates, is outlined. An overview of the Doppler cooling and magneto-optical trapping techniques used to create cold gas clouds is given. RF evaporative cooling, which is used to create very cold and dense clouds, is discussed. Finally, a method of measuring the temperature of a cold cloud by ballistic expansion is detailed.

2.2 Magnetic trapping

A paramagnetic atom has a permanent dipole moment and can be trapped in an inhomogeneous magnetic field. Atom chips rely on magnetic trapping, so the major atom chip review articles contain good descriptions of magnetic trapping [21], [22].

2.2.1 Magnetic potential

Interactions between atoms and magnetic fields are described in most atomic physics texts, including Ref. [23]. A magnetic dipole $\vec{\mu}$, when placed in a magnetic field $\vec{B}$, has an interaction energy

$$V_B = -\vec{\mu} \cdot \vec{B}. \tag{2.1}$$

An atom in a given state with total atomic angular momentum $\vec{F}$ and a corresponding Landé factor g_F will have a magnetic dipole moment

$$\vec{\mu} = \mu_B g_F \vec{F} \tag{2.2}$$

and a magnetic field interaction energy

$$V_B = -\mu_B g_F \vec{F} \cdot \vec{B}, \tag{2.3}$$

where μ_B is the Bohr magneton.

In the adiabatic limit, where the change in the direction of $\vec{B}$ is much slower than the Larmor frequency

$$\omega_L = \mu_B B/\hbar, \tag{2.4}$$

the dipole moment follows the magnetic field. The magnetic quantum number m_F, defined as the scalar projection of $\vec{F}$ onto the axis of quantization defined by $\vec{B}$, is constant. In this case, the magnetic interaction energy will be a conservative potential, given by

$$V_B = -\mu_B g_F m_F B. \tag{2.5}$$

Depending on the sign of g_F and the magnitude and sign of m_F, three scenarios are

possible:

- $\frac{dV_B}{dB} = 0$. This occurs if $m_F = 0$. The potential energy of an atom in an $m_F = 0$ state does not depend on the magnetic field, so it cannot be magnetically trapped.

- $\frac{dV_B}{dB} < 0$. Local minima in the potential occur at local maxima of the magnetic field, so these states are called *strong-field seeking*. Local magnetic field maxima cannot exist in free space, however, according to Earnshaw's theorem [21]. Thus purely magnetostatic trapping of an atom in a strong-field seeking state is not possible.

- $\frac{dV_B}{dB} > 0$. Local minima in the potential occur at local minima of the magnetic field and these states are called *weak-field seeking*. An atom in a weak-field seeking state can be trapped in a magnetic field minimum generated by a purely magnetostatic trap (magnetic field minima can occur in free space).

Atoms in weak-field seeking states can only be trapped in non-zero minima of the magnetic field. As an atom approaches a region with zero (or sufficiently small) magnetic field, the adiabatic limit is no longer satisfied (since the Larmor frequency will become very small) and $\vec{\mu}$ will no longer follow the magnetic field. The orientation of $\vec{F}$ with respect to $\vec{B}$ may change, with the result that the atom ends up in a different m_F sublevel, which may be an untrapped state.

Thinking in terms of the energies of the states involved, all of the m_F sublevels are degenerate at $B = 0$, so an avoided crossing is created. At the avoided crossing, non-adiabatic Majorana transitions or spin-flips from the trapped weak-field seeking states to untrapped states can occur. Atoms which are not in weak-field seeking states quickly fall or accelerate out of the trap and are lost. As a result, cold atoms confined in magnetic traps must not go near regions of zero magnetic field. Fig. 2.1

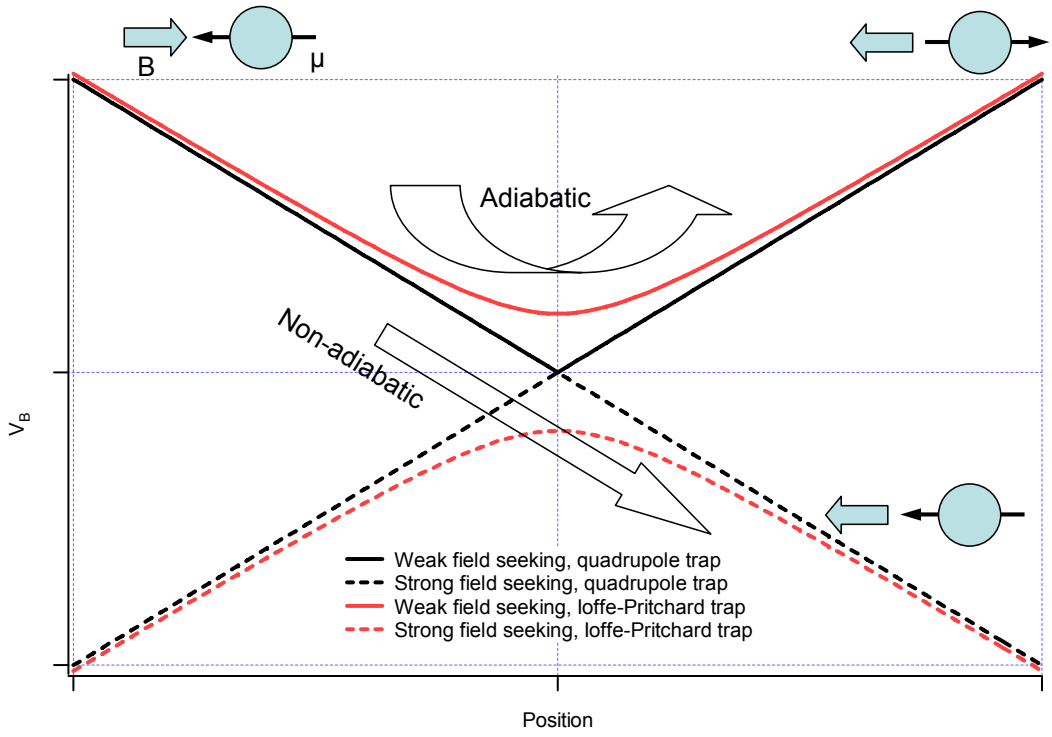

Figure 2.1: An atom in a weak-field seeking state (g_F is presumed to be positive in this diagram) nears a magnetic field minimum. The atom's magnetic moment may adiabatically follow the field direction, or undergo a non-adiabatic (Majorana) transition to a strong-field seeking state. Non-adiabatic transitions are likely if the atom goes through a magnetic field zero, such as exists in a quadrupole trap.

illustrates the differences between a magnetic quadrupole trap with a field zero, and a Ioffe-Pritchard trap with a non-zero field minimum.

2.2.2 Side guides and Ioffe-Pritchard traps

One way to create high field gradients is the 'side guide' formed near a long current-carrying wire, a geometry proposed by Frisch and Segrè in 1933 [21]. The geometry is shown in Fig. 2.2. A long straight wire carrying current I generates a magnetic field

$$B_w = \frac{\mu_o I}{2\pi r}, \tag{2.6}$$

where r is the distance from the wire. If the wire is placed in a homogeneous magnetic *bias field* B_b perpendicular to the wire, the fields cancel each other exactly at a distance

$$z_o = \frac{\mu_o I}{2\pi B_b}, \tag{2.7}$$

and weak-field seeking atoms can be guided along the field zero (This geometry is a 2-D quadrupole, so it is a guide rather than a trap). The magnetic field gradient near the field zero is easily shown to be

$$\frac{\partial B}{\partial r}|_{z=z_o} = -\frac{\partial B_w}{\partial r}|_{z=z_o} = \frac{\mu_o I}{2\pi z_o^2}. \tag{2.8}$$

Since the magnetic field gradient near the field zero scales as $1/z_o^2$, high field gradients are found close to the wire. Reducing the size of the wire allows the trap to be created closer to the wire center. However, the maximum current depends on the wire size. Taking the wire to be a cylinder of radius R, the current is $I = \pi R^2 J$, where J is the current density. The minimum possible z_o is on the order of R. Thus

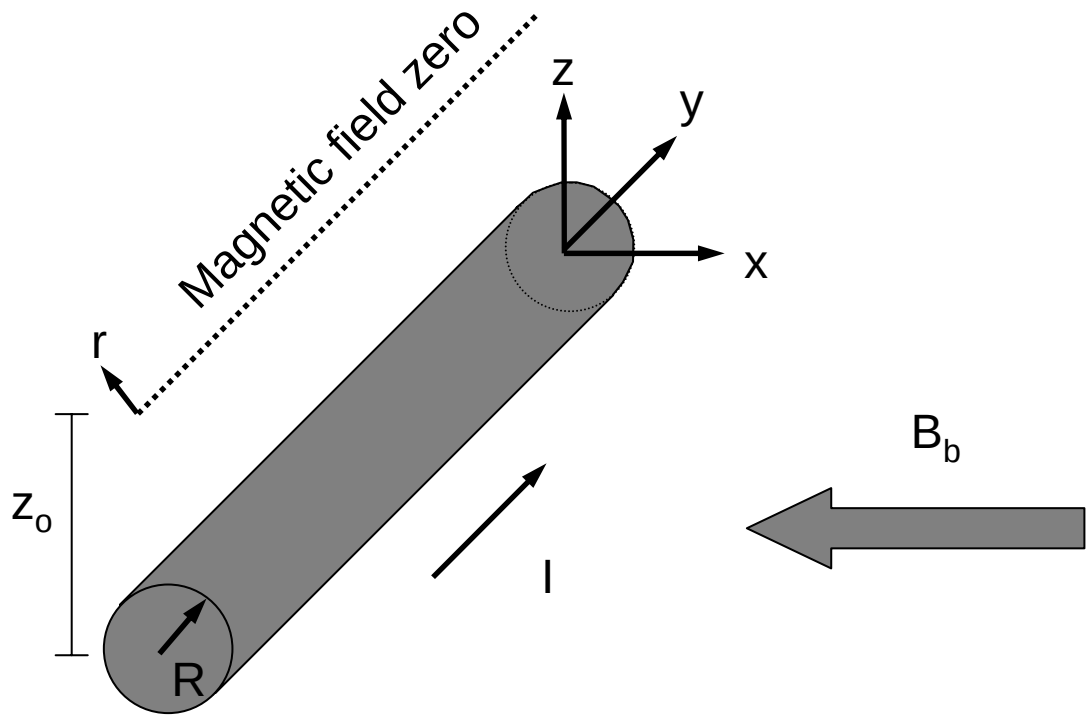

Figure 2.2: Side guide, used to confine weak-field seeking atoms. B_b and the field from the current-carrying wire cancel each other a distance z_o from the wire center.

the maximum possible field gradient for a cylindrical wire is given by

$$\frac{\partial B}{\partial r}|_{z=z_o} = \frac{\mu_o J R^2}{2 z_o^2} \propto J \tag{2.9}$$

and is not explicitly dependent on R but only J. Despite this, smaller wires can create higher field gradients than large wires because the maximum possible current density is larger for small wires. This is because the larger surface area/volume ratio of small wires allows for faster heat transfer out of the center of the wire.

True 3-D trapping can be achieved by sealing the ends of the guide. The simplest way is to bend the straight wire into a Z shape, with the leads in the plane of B_b. The axial magnetic fields created by the leads add to create a non-zero field along the entire length of the trap minimum. The magnetic field increases near the leads, so that atoms are confined in the axial direction. The shape of the potential near the minimum changes from a linear gradient to a harmonic potential. The superposition of an axial magnetic field on a quadrupole trap with sealed ends is known as a Ioffe-Pritchard trap [24]. The term 'Ioffe-Pritchard trap' is also used more generally by some authors to describe any magnetostatic trap with a non-zero harmonic minimum [20].

Bending the wire leads into a U shape will also create a 3-D trap, but the trap will have a quadrupole zero since the axial fields generated by the leads will cancel each other at the center of the U. Quadrupole fields have their uses, particularly in magneto-optical traps, and in fact the quadrupole field of the magneto-optical trap in our experiment is generated using a macroscopic U-shaped current carrying wire in a bias field.

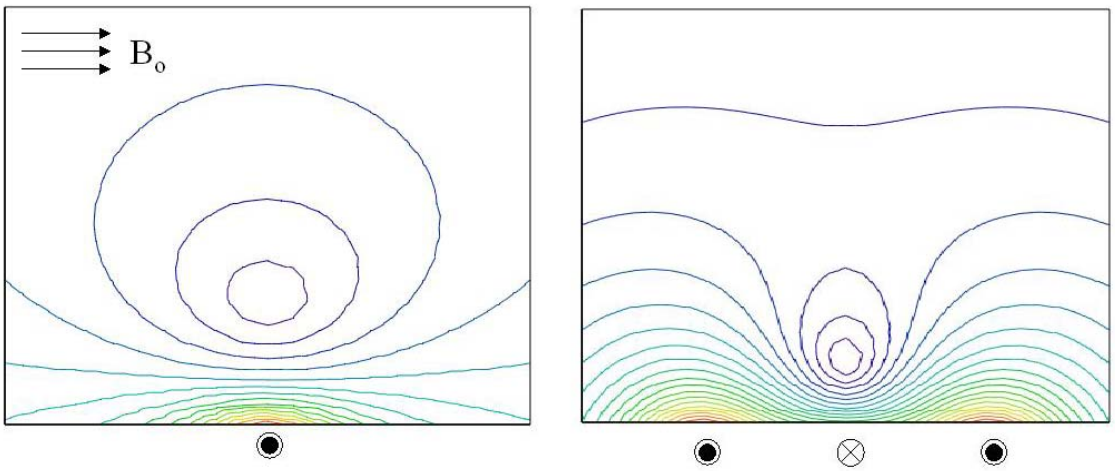

Figure 2.3: Magnetic field contours for 1-wire (left) and 3-wire (right) trapping geometries. The wires are perpendicular to the plane of the figure, with currents running in the directions indicated.

2.2.3 Atom chips

The Z-wire geometry lends itself well to miniaturization because of the planar geometry of the trap. The wire can be mounted on a substrate, for better mechanical rigidity and higher current density (heat from electrical resistance will be conducted into the substrate). Microfabrication techniques developed for the semiconductor industry can be employed to define wire patterns on the substrate with dimensions of less than 1 μm. The resulting device is referred to as a magnetic microtrap [17] or atom chip [18]. Excellent review articles have been written by Folman *et al.* [21] and Fortagh and Zimmerman [22]. Atom chips are useful for studying interactions between atoms and surfaces. The distance between the atoms and the surface can be precisely varied by adjusting the current and the bias field. The high field gradients also give stronger confinement (smaller clouds) so that the atom-surface distance is more uniform than would be the case for a trap made with macroscopic current-carrying structures.

For atom-wire distances of less than 10 μm, the bias fields required are typically

hundreds of Gauss, even for relatively modest wire currents of a few hundred mA. The Helmholtz coils needed to produce fields of such strength can be impractically bulky and have high inductance. Instead, the bias field can be produced by additional parallel wires on the chip surface, carrying currents in the opposite direction to the center wire. A three-dimensional trap can be created entirely with wires on the chip surface. Note that for clouds very close to the surface compared to the length of the trap, the axial field produced by the wire leads may be too small to suppress trap losses due to Majorana transitions. In this case, an axial field of a few Gauss may have to be applied with external coils. The shapes of the trapping potentials generated in these two geometries are compared in Fig. 2.3.

2.3 Magneto-optical trapping

Neutral atoms interact quite weakly with magnetic fields, so practical atom chips have trap depths of at most a few mK. A source of cold atoms must be used to load the chip. Atom chip experiments typically use vapor-cell magneto-optical traps (MOTs) to produce large ($\sim 10^6 - 10^9$) clouds of cold atoms [19]. The characteristics of MOTs can be most easily explained using an idealized two-level atom, with the energy structure shown in Fig. 2.4. A good reference book has been written by Metcalf and van der Straten [25].

Magneto-optical traps use Doppler cooling to introduce a velocity-dependent damping force. A laser beam is red-detuned (lower frequency) from the transition. In the reference frame of an atom moving toward the beam, the beam will be Doppler-shifted into resonance so that the atom will absorb a photon. The atom will then emit a photon in a random direction, so that over repeated scattering events, it receives many momentum kicks in the direction of the beam and slows down. In the reference frame of an atom moving away from the beam, the light will be Doppler-shifted even

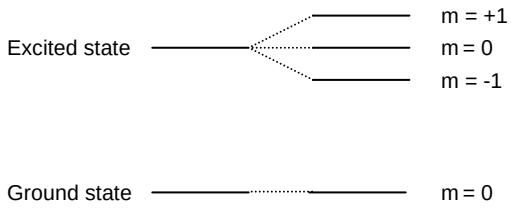

Figure 2.4: Idealized atomic structure for magneto-optical trapping. The transition is closed (all the excited states decay down to the ground state) and the upper energy level is split by the Zeeman effect.

farther out of resonance so that an atom moving away from the beam will not scatter photons. Adding a second counterpropagating beam creates a 1-dimensional optical molasses—an atom will preferentially absorb photons from the beam it is moving toward, experiencing a velocity dependent damping force in the direction opposite of its motion. Two more pairs of counterpropagating beams will create a 3-D optical molasses, in which atomic motion in any arbitrary direction is damped. Doppler cooling is illustrated in Fig. 2.5.

Position-dependent forces are also possible. A circularly polarized laser beam propagating along a magnetic field can excite either σ^+ or σ^- transitions, depending on its orientation relative to the magnetic field. If the laser beam propagates through a quadrupole zero, the orientation of the polarization with respect to the field is reversed, so that the beam can excite only σ^+ transitions on one side of the quadrupole zero and only σ^- transitions on the other. Due to the Zeeman effect, the σ^+ transitions will be blue-detuned and the σ^- transitions will be red-detuned. A laser which is red-detuned from the atomic resonance (for Doppler cooling) will preferentially excite σ^- transitions. Choosing the correct circular polarization with respect to the magnetic field direction, the beam will excite σ^- transitions in atoms between the laser and the

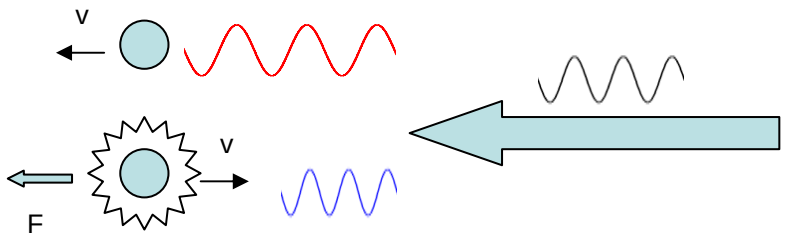

(a)

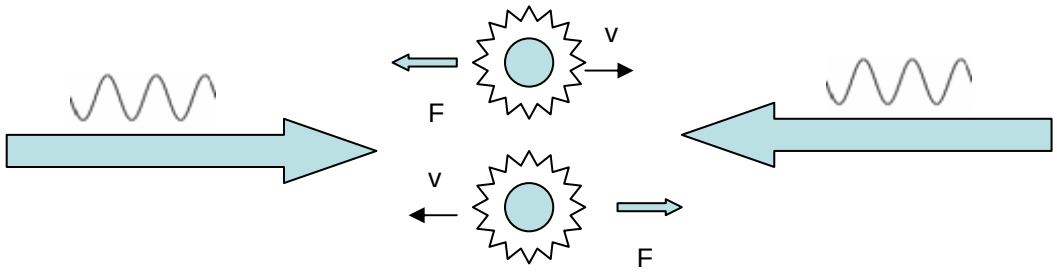

(b)

Figure 2.5: (a): A single laser beam is detuned to the red of an atomic transition. The Doppler effect will red-shift the light out of resonance if an atom is moving away from the beam, but blue-shift the light into resonance if the atom is moving toward the beam. An atom moving toward the beam will absorb photons from the beam and experience a net force in the direction opposing its motion.

(b):1-D optical molasses, with two counterpropagating red-detuned beams.

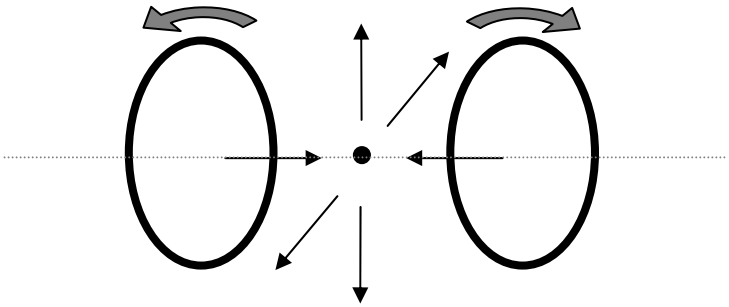

(a)

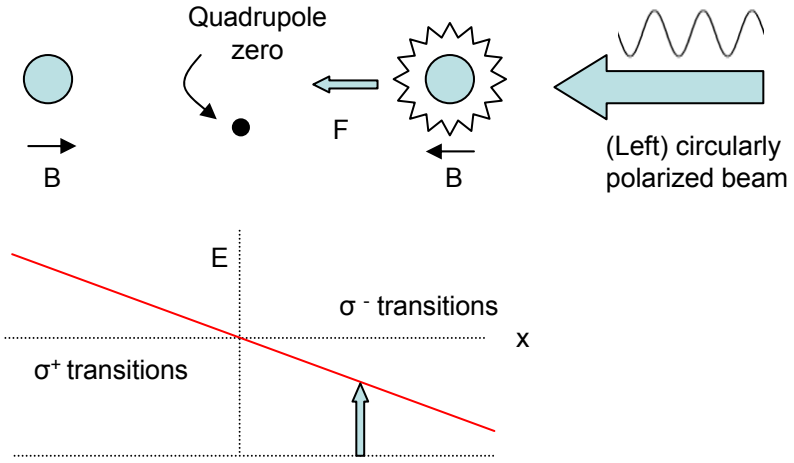

(b)

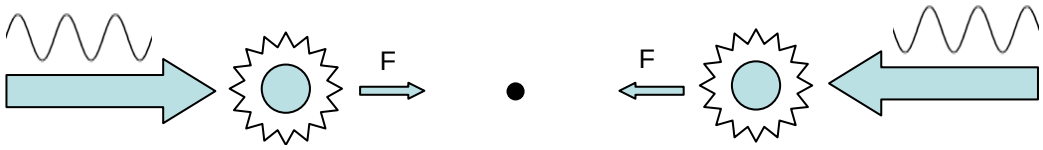

(c)

Figure 2.6: (a): A magnetic quadrupole zero formed by running current through two coils in "anti-Helmholtz" configuration.

(b): A single circularly polarized laser beam (left circularly polarized for the field configuration shown) passing through the quadrupole zero is red-detuned from an atomic transition. Because of angular momentum selection rules, the beam can excite σ^+ transitions on the left side of the field zero and σ^- transitions on the right. The beam is only resonant with the Zeeman-shifted σ^- transitions, so atoms on the right side of the quadrupole zero absorb photons and are forced toward the quadrupole zero.

(c): 1-D MOT, with two counterpropagating beams.

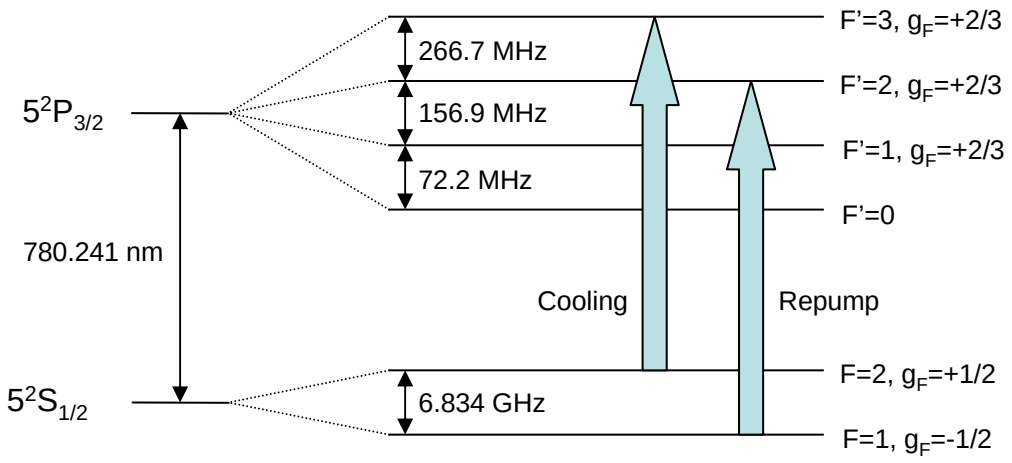

Figure 2.7: Hyperfine structure of the $5^2S_{1/2}$ and $5^2P_{3/2}$ levels of ^{87}Rb (data from Ref. [26]). The cooling laser excites the $F = 2 \rightarrow F' = 3$ transition, and the repump laser excites the $F = 1 \rightarrow F' = 2$ transition.

quadrupole zero, and the atoms absorb photons and are pushed toward the quadrupole zero. If a second counterpropagating beam is added, atoms on both sides of the quadrupole zero will be pushed toward the quadrupole zero. Two more pairs of counterpropagating beams will create a 3-D magneto-optical trap, in which atoms displaced from the quadrupole zero in any direction are forced toward the quadrupole zero as they absorb and emit photons. Magneto-optical trapping is illustrated in Fig. 2.6.

Most atomic species cooled in MOTs cannot be treated as two-level systems, and their hyperfine structure must be taken into account. For example, the atomic transition used to cool ^{87}Rb in a MOT is from the $5^2S_{1/2}$ ground state to the $5^2P_{3/2}$ excited state, shown in Fig. 2.7. The ground state has two hyperfine levels ($F = 1, 2$) and the excited state has four ($F = 0, 1, 2, 3$). The cooling laser can be used to excite the $F = 2 \rightarrow F' = 3$ transition, which is convenient because the only dipole-allowed decay from the $F' = 3$ excited state is back to the $F = 2$ ground state, allowing one

atom to scatter many photons and cool down. However, atoms may end up in the $F = 1$ ground state if the cooling laser excites the nearby $F = 2 \rightarrow F' = 2$ transition or through dipole-forbidden decay from the $F' = 3$ excited state. Atoms in the $F = 1$ ground state do not interact with the cooling laser and tend to be lost from the MOT so a repump laser is needed to excite the $F = 1 \rightarrow F' = 2$ transition and keep population from building up in the $F = 1$ state.

2.4 RF evaporative cooling

The cloud of cold atoms generated by the MOT is too large and too hot to be efficiently loaded into the magnetic microtrap. Further cooling and compression of the trap is required. This is done by transferring the atoms into a macroscopically sized magnetic trap and applying RF evaporative cooling. A good review paper has been written by Ketterle and van Druten [20].

The entire cloud can be cooled by selectively removing the atoms with the highest energy. This can be accomplished by reducing the depth of the potential well to the point where the most energetic atoms can escape the trap completely. In magnetic traps, RF evaporative cooling is a convenient method for reducing the well depth without changing the geometry of the trapping potential. Transitions from weak-field seeking to strong-field seeking states are in the RF frequency range, so that atoms can be removed from the trap by applying RF. The frequency of the transition depends on the local magnetic field (and thus the potential energy of the atom). The RF can thus be tuned to remove the most energetic atoms. As the cloud cools, the RF frequency is decreased to continue the cooling process.

As the most energetic atoms are removed, the remaining energy is redistributed through a series of elastic collisions between the remaining atoms. The speed of this rethermalization depends on the rate of elastic collisions between atoms, given by

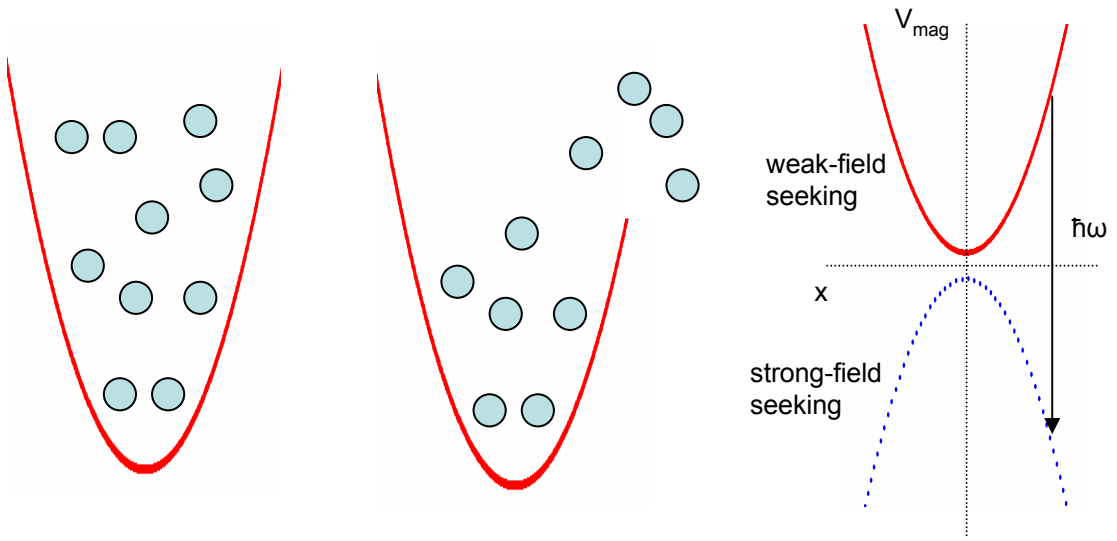

Figure 2.8: Evaporative cooling of atoms trapped in a harmonic potential (left) is performed by reducing the well depth to allow the most energetic atoms to escape (center). This is typically done by applying RF to stimulate transitions from weak-field seeking states to strong-field seeking states (right).

$\eta\sigma v$, where η is the number density per unit volume, σ is the s-wave scattering cross section of the atom, and v is the mean velocity. As a cloud is cooled, v decreases but η increases. During cooling $\eta\sigma v$ should stay constant or increase (a situation known as runaway evaporation), in order to have a substantial population of cold atoms left at the end of the process. If the rate of elastic collisions is not large enough compared to the rate of 'bad' collisions (losses due to background gas collisions and inelastic three-body collisions), runaway evaporative cooling is not possible [20].

As a magnetically trapped cloud of atoms is adiabatically compressed, the temperature increases so that η and v increase. Tightly confining traps thus maximize the elastic collision rate. RF evaporative cooling to BEC has been achieved in less than one second in an atom-chip trap [27]. However, the rate of inelastic three-body collisions, which cause both atom loss and trap heating, grows as η^2, so strongly confining traps can actually reduce the efficiency of evaporative cooling for very large

clouds (10^9 atoms) [28].

The cooling process is most efficient if the speed of the RF frequency sweep is matched to the elastic collision rate, which increases as the cloud cools. The RF frequency is typically changed in a series of linear sweeps, with the duration, sweep rate and RF power during each step optimized by experiment.

2.5 Temperature measurement

The temperature of a cloud of trapped atoms can be measured through ballistic expansion—turning off the confining potential quickly and allowing the cloud to freely expand. If the atoms are not accelerated during the expansion, the velocity of an atom is constant during the expansion and its position $\vec{r}(t)$ at time t is given by

$$\vec{r}(t) = \vec{r_o} + \vec{v}t, \tag{2.10}$$

where $\vec{r_o}$ is the position of the atom at the instant before the expansion ($t = 0$) and $\vec{v}$ is the velocity. If all of the atoms accelerate uniformly (due to gravity, for example) this equation is still valid to describe the position relative to the center of mass of the cloud.

The initial position and velocity are characterized by probability distributions $f_{r_o}(\vec{r_o})$ and $f_v(\vec{v})$, respectively. If these distributions are uncorrelated, then the position distribution f_r at a given time t is given by the convolution

$$f_r(\vec{r}, t) = \int d^3r f_{r_o}(\vec{r_o}) f_v(\frac{\vec{r} - \vec{r_o}}{t})t. \tag{2.11}$$

If a classical gas is in thermal equilibrium, the velocity distribution is a spherical 3-D

Gaussian in momentum space (the Maxwell-Boltzmann distribution), so

$$f_v(v_x, v_y, v_z) = A_v^3 e^{-(\frac{v_x^2}{2\sigma_v^2}+\frac{v_y^2}{2\sigma_v^2}+\frac{v_z^2}{2\sigma_v^2})}, \tag{2.12}$$

subject to the normalization condition

$$\int d^3v f_v(\vec{v}) \equiv 1 \tag{2.13}$$

and the equipartition theorem

$$\frac{1}{2}M < v_x^2 >= \frac{1}{2}k_B T \tag{2.14}$$

(and similarly for v_y and v_z), where M is the atomic mass and k_B is Boltzmann's constant. This yields the result

$$\sigma_v^2 = \frac{k_B T}{M}. \tag{2.15}$$

If the trapping potential is a 3-D harmonic oscillator, $f_{\vec{r}_o}(\vec{r_o})$ is a 3-D Gaussian (not in general spherically symmetric), given by

$$f_{r_o}(\vec{r_o}) = A_{r_o} e^{-(\frac{x^2}{2\sigma_x^2}+\frac{y^2}{2\sigma_y^2}+\frac{z^2}{2\sigma_z^2})}. \tag{2.16}$$

A_r,σ_x,σ_y and σ_z can be calculated in the same way as A_v and σ_v but their exact values are not important for measuring the cloud temperature with ballistic expansion. The convolution

$$f_r(\vec{r}, t) = Ae^{-\frac{1}{2}(\frac{x^2}{\sigma_v^2 t^2+\sigma_x^2}+\frac{y^2}{\sigma_v^2 t^2+\sigma_y^2}+\frac{z^2}{\sigma_v^2 t^2+\sigma_z^2})} \tag{2.17}$$

shows that the cloud expands in a 3-D Gaussian shape, and the width σ_x along the

x-axis evolves in time as

$$\sigma_x^2 = \sigma_{x_o}^2 + \sigma_v^2 t^2 = \sigma_{x_o}^2 + \frac{k_B T}{M} t^2. \tag{2.18}$$

A series of images of the cloud can be taken at different points during the free expansion and the widths σ_x and σ_y can be determined by fitting to 2-D Gaussians. A plot of σ_x^2 vs. t^2 will be linear with a slope of $\frac{k_B T}{M}$, as given in Ref. [29], so that the temperature of the cloud can be determined. In the absence of spatially non-uniform acceleration of the atoms, the calculated temperature will be the same regardless of the axes chosen for imaging and fitting.

Chapter 3

Design & Implementation

3.1 Overview

This chapter describes the design and construction of the experimental setup. The design, construction, and preparation of the ultrahigh vacuum system are discussed and the performance of the system is evaluated. The design and construction of the coils and macroscopic current-carrying structures are described. The design and construction of the first and second generation atom chips are discussed, including calculations of the expected trapping parameters. The laser systems used for the MOT and imaging are described, including the frequency-locking schemes. The cameras and imaging systems are detailed, including a discussion of the procedures for absorption imaging and measuring the number of trapped atoms. The RF evaporative cooling scheme is described. Finally, the experiment control hardware and software are discussed.

The main chamber design is very similar to the chamber used to study Rydberg atoms in free space, located next door in lab 140 [30]. The geometry of the MOT and the loading of the atom chip are patterned after the successful apparatus of Ref. [31]. Some equipment specific to Rydberg atom experiments has been added, most

notably plates to generate electric fields for field ionization and a microchannel plate detector to detect the ionized atoms. The main vacuum chamber is stainless steel and is considerably larger than the glass cells used in most atom chip experiments due to the extra equipment required. Glass cells are prone to accumulating charge and creating stray electric fields which make Rydberg atom experiments difficult, so a grounded stainless steel chamber is better. However, optical access is severely limited compared to a glass cell and the coils to generate magnetic fields must be mounted farther away from the trap, limiting the maximum magnetic fields and gradients which can be conveniently produced with coils.

A conventional 6-beam MOT cannot be formed near the chip because the chip limits optical access. Therefore, atom chip experiments using a 6-beam MOT as a source of cold atoms either transport the atoms from the MOT toward the chip surface in a movable magnetic trap [32] or with optical tweezers [33]. These approaches are difficult to implement inside the chamber used in this experiment due to the large size of the chamber and limited optical access. However, fabricating the chip so that the surface is an optical-quality reflector allows the loading of the chip from a four-beam mirror MOT [17], which is relatively easy to implement in our chamber geometry.

Strongly confining magnetic microtraps allow RF evaporative cooling to be done efficiently in periods as short as a few seconds [27], [16]. Thus, the vacuum requirements for atom chip experiments are not particularly severe. For example, with a 10^{-9} Torr room-temperature background of hydrogen, the lifetime of trapped rubidium can be calculated to be about 20 s—easily long enough to perform efficient evaporative cooling [21].

With this in mind, a single-chamber system was chosen, rather than the more complex two-chamber differentially pumped designs which are more common in AMO experiments. The vapor-cell MOT is loaded with room-temperature ^{87}Rb atoms which

are released into the chamber from a dispenser. Thus, high ^{87}Rb partial pressures are desirable for fast loading and large clouds of trapped atoms but create unwanted background collisions which reduce the trap lifetime in the later phases of the experiment. Selecting the ideal pressure of Rb in the chamber is a matter of compromise.

3.2 Ultrahigh Vacuum System

3.2.1 Design and components

The main experimental chamber is a spherical octagon (Kimball Physics MCF600-SO200800-A), shaped like a cylinder with two 6-inch diameter flanges facing each other and eight 2 3/4-inch flanges around the circumference. The chip is mounted facing down in the center of the chamber. Because of the size of the electrical connectors required, the chip is mounted on a 4 5/8-inch flange, connected to the chamber via a conical reducer, and extends through the top hole in the main chamber.

Six viewports are required, as shown in Fig. 3.1: Four viewports for the MOT beams and two for the absorption imaging beamline. A beam for optical pumping also enters the chamber via the absorption imaging beamline. Also, a laser beam for excitation of the atoms to Rydberg states (480 nm) will enter the chamber through the large front viewport. The imaging beam and axial viewports are all fused silica, to allow for the possibility of efficient photo-desorption of rubidium in the chamber with a 355 nm wavelength frequency-tripled Nd:YAG pulse. Direct excitation of Rydberg states from the ground state with a 297 nm wavelength excitation source would also be possible. The viewports for the radial beams are borosilicate glass, and are antireflection coated for 780 nm since most of the optical power in the MOT beams passes through these viewports.

There are three pumps in the system: Two 20 L/s triode ion pumps (Duniway

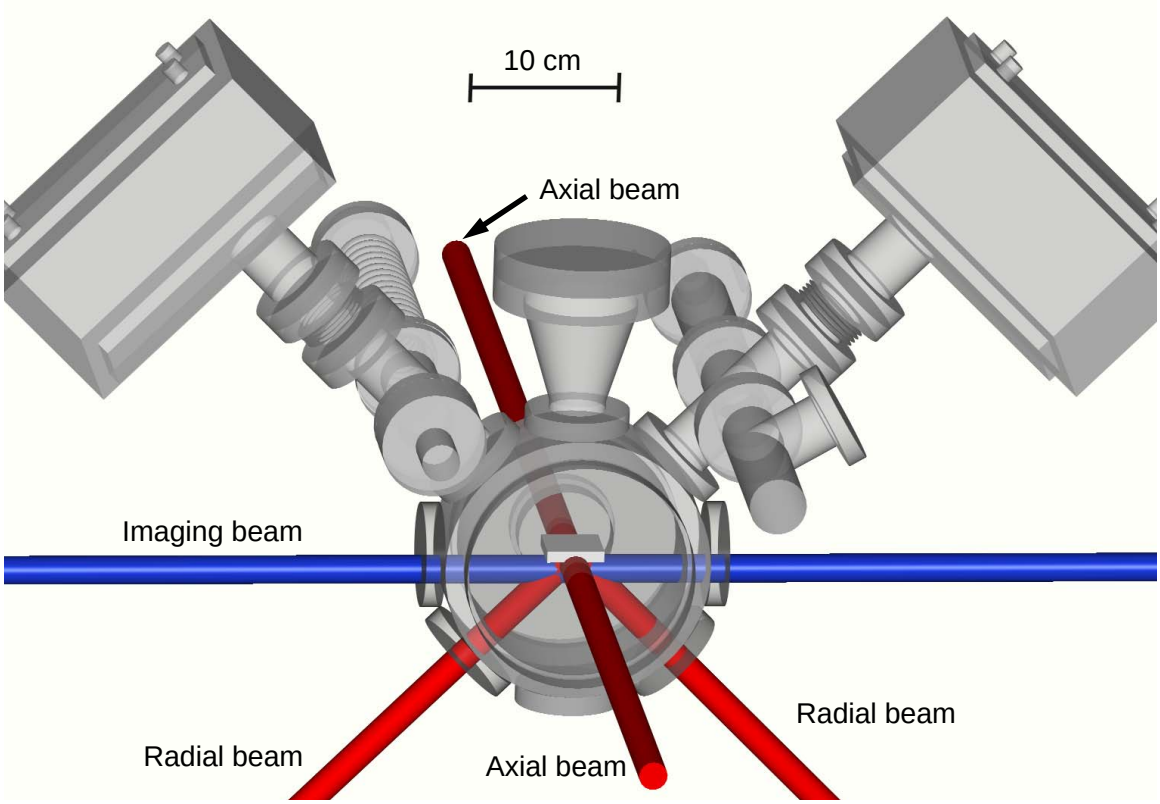

Figure 3.1: Schematic of the vacuum chamber optical access, showing the four MOT beams and the absorption imaging beamline (additional beams for optical pumping, Rydberg excitation, and photo-desorption not shown here).

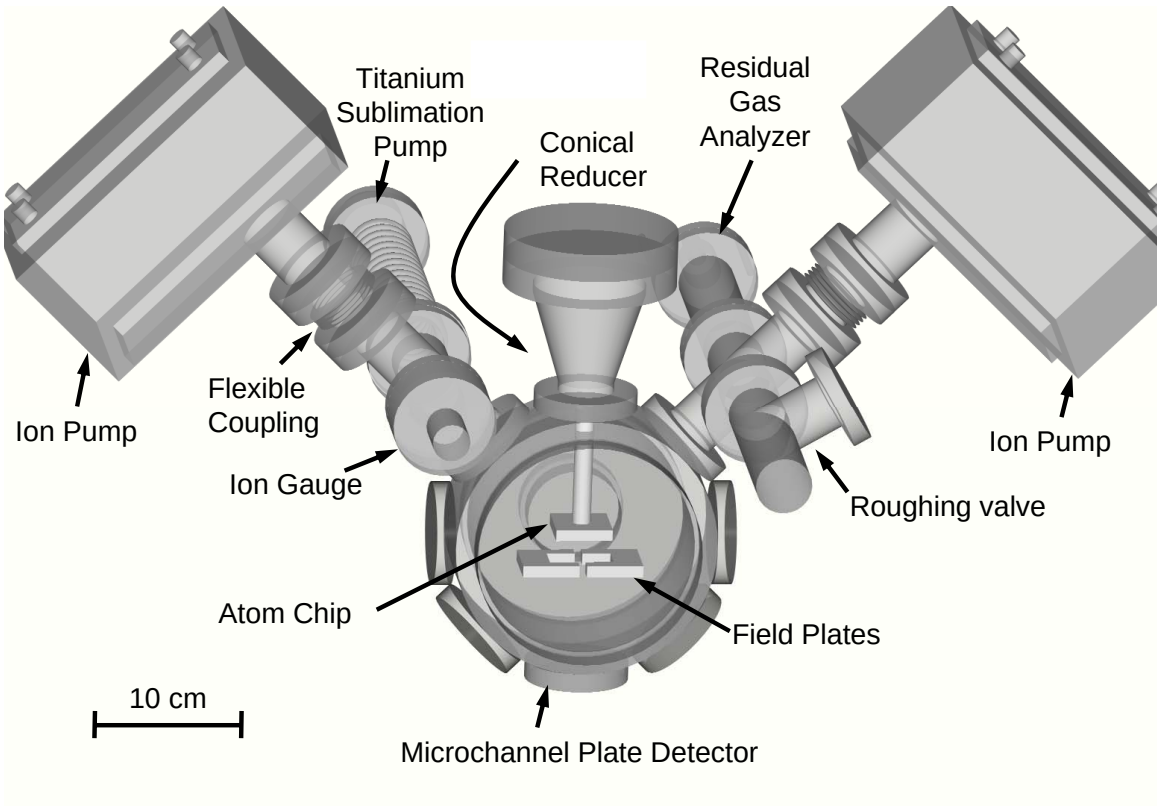

Figure 3.2: Schematic of the vacuum chamber, showing the locations of various components.

Stockroom) and a single titanium sublimation pump (Duniway Stockroom). The ion pumps run continuously, while the titanium sublimation pump is only run every few months, when the background pressure in the chamber becomes too high to conveniently perform experiments. To measure the pressure and background gas composition in the chamber, an ion gauge (Duniway Stockroom) and residual gas analyzer, or RGA (Stanford Research Systems) are also included. The pumps, gauge and RGA are connected to the chamber via tee crosses as shown in Fig. 3.2. The pumps and tee crosses are securely bolted to an aluminum frame and are connected to each other with flexible bellows to avoid excessive mechanical strain during bakeout.

The RGA was invaluable during the initial pump-down phase of the experiment. Several leaks were encountered around the 2 3/4-inch flanges on the chamber, which

needed an unexpectedly high amount of torque on the bolts to properly seal. The ability of the RGA to identify specific atomic masses (such as argon or helium) made leak checking much easier. The RGA is a good tool for identifying the components of the gas present in the chamber and measuring their relative abundance. However, it is not as useful for measurements of absolute pressure because it tends to increase the background pressure in the chamber (by approximately 5×10^{-9} Torr) whenever it is turned on for long periods of time. The RGA has never been baked out at its recommended bakeout temperature of 200°C, which would not be practical for this setup. This probably contributes to the gas load produced.

In day-to-day operation, the ion gauge is used to measure the pressure of the chamber. No measurable increase in the background pressure has been observed during ion gauge operation. The absolute accuracy of an ion gauge is typically ±20%. Additionally, the gauge sensitivity depends on the background gas, as small atoms are more difficult to ionize. The gauge is calibrated for nitrogen, while the dominant background gas is hydrogen. Thus, ion gauge readings must be divided by a correcting factor (0.46) to arrive at the proper absolute measurement of the hydrogen background pressure [34]. Given the uncertainties in the gauge sensitivity and background gas composition at the gauge (the RGA is quite a distance away), taking the uncertainty of absolute pressures measured by the gauge as 30% seems reasonable. Even then, this number will be influenced by the geometry of the chamber and will not necessarily be the same as the background pressure at the trap. In any case, the lifetime of the magnetically trapped atom cloud is by far the most important measure of the pressure.

To supply the rubidium vapor for cooling and trapping, six dispensers (SAES Getters) were mounted in the chamber. The dispensers produce rubidium vapor through the chemical reduction of rubidium chromate, which occurs when they are heated to

several hundred degrees Celsius by passing several amperes of current through each dispenser. The dispensers are mounted in two sets, with each set consisting of three dispensers electrically in parallel. Only one set is used at a time. Based on previous experience in lab 140 , we assume that these dispensers contain enough rubidium to supply the MOT for several years. The rubidium in the dispensers is not isotopically enriched, so only about 25% of the rubidium dispensed is ^{87}Rb. The remainder is ^{85}Rb, which simply adds to the background gas load in the chamber.

3.2.2 Preparation

Machined parts were put through the following cleaning procedure, derived from the procedure used for the chamber in lab 140, described in Ref. [30].

1. The parts were ultrasonically cleaned in hot soapy water for about half an hour, then rinsed with distilled water to remove the soap and blown dry with pressurized argon (clean compressed air or nitrogen would have worked just as well; we just happened to have a cylinder of argon).

2. The remaining machining oil on the parts was removed by ultrasonically cleaning in trichloroethylene for half an hour and then blowing dry as in the first step.

3. Oxidation on the copper pieces was removed by soaking in room-temperature 5% acetic acid for about one hour. The copper pieces were then rinsed several times in distilled water to remove the acid and then blown dry.

4. The parts were ultrasonically cleaned in acetone for half an hour to further remove organic contamination and then blown dry.

5. Finally, the parts were ultrasonically cleaned for 15 minutes in HPLC-grade isopropanol and blown dry.

Between cleaning steps, the parts were stored inside a sealed dry box to avoid dust contamination and to slow oxidation of the copper parts. After the initial cleaning in soapy water, the parts were handled only while wearing nitrile gloves to avoid contamination from fingerprints. The tools used to assemble the interior parts of the chamber were also cleaned using the above procedure.

Commercially supplied vacuum components had the conflat knife-edges cleaned with an isopropanol-soaked clean room wipe prior to assembly. In addition, the windows of the viewports were thoroughly cleaned with methanol and/or isopropanol and lens tissues. These components were already quite clean on delivery (and were always handled while wearing clean nitrile gloves) so rigorous cleaning was not required and would have only increased the likelihood of contamination.

Roughing the chamber was done with a Roots blower and cryo-sorption pump (Perkin-Elmer). The Roots blower stage reduced the chamber pressure from atmosphere to an estimated pressure of a few Torr (no gauge in the system can measure pressures that high directly). The two stages of the cryosorption pump reduced the pressure to 1.5×10^{-1} Torr and 2.2×10^{-2} Torr, respectively, measured with a thermocouple vacuum gauge (Duniway Stockroom). When the pressure in the chamber stabilized, the ion pumps were started and the roughing valve was then closed. The ion pumps reduced the chamber pressure to 2×10^{-4} Torr (calculated by the pump controller using measurements of the current and operating voltage) within a few minutes and to 2×10^{-7} Torr (again measured with the pump controller) within a day.

The chamber was baked to a temperature of 120°C to desorb contaminants such as water, CO, and CO_2. The bakeout was done by moving the entire chamber into an oven constructed for this purpose. Two bakeouts cycles were performed. In the first, the chamber was held at 110°C for 12 hours and then 120°C for 24 hours. In

the second, the chamber was held at 120°C for a further 85 hours. Care was taken to ramp the oven temperature slowly at the beginning and end of the bakeout cycles to allow the chamber to heat up and cool down evenly. The bakeout temperature is limited by the insulating material (nylon) used to create electrical breaks in the square coils, and the insulation on the electrical connectors for the coils. Mounting the coils after bakeout is not an option as they must be positioned in the frame before final chamber assembly. Materials tolerant of higher temperatures would lead to slightly better bakeout, but the construction of the oven and the temperature limits of the ion pump magnets limit bakeout temperatures to 150°C in any case.

The chamber pressure during the bakeout was measured with the ion gauge, and the chamber temperature and pressure during the bakeout cycles are plotted in Figs. 3.3 and 3.4. Two days after the end of each bakeout, the indicated pressure was approximately 5×10^{-9} Torr.

3.2.3 Performance

Two weeks after the second bakeout the indicated pressure was 6.0×10^{-10} Torr, which given the gauge accuracy and correction factor, corresponds to a chamber base pressure of $1.3 \times 10^{-9} \pm 0.4 \times 10^{-9}$ Torr. When the MOT is in daily operation, the indicated pressure is typically around 2×10^{-9} Torr at the start of the day. The dispensers are operated continuously with 18 A of current (running through three dispensers connected electrically in parallel). This causes enough power dissipation to noticeably warm the vacuum chamber so that over the course of the day the indicated pressure increases to around $4 - 6 \times 10^{-9}$ Torr. The background pressure in the chamber is thus on the order of 10^{-8} Torr during experiments. At this pressure, trap 1/e lifetime is limited to about 2 s by collisions with hot background gas in the chamber.

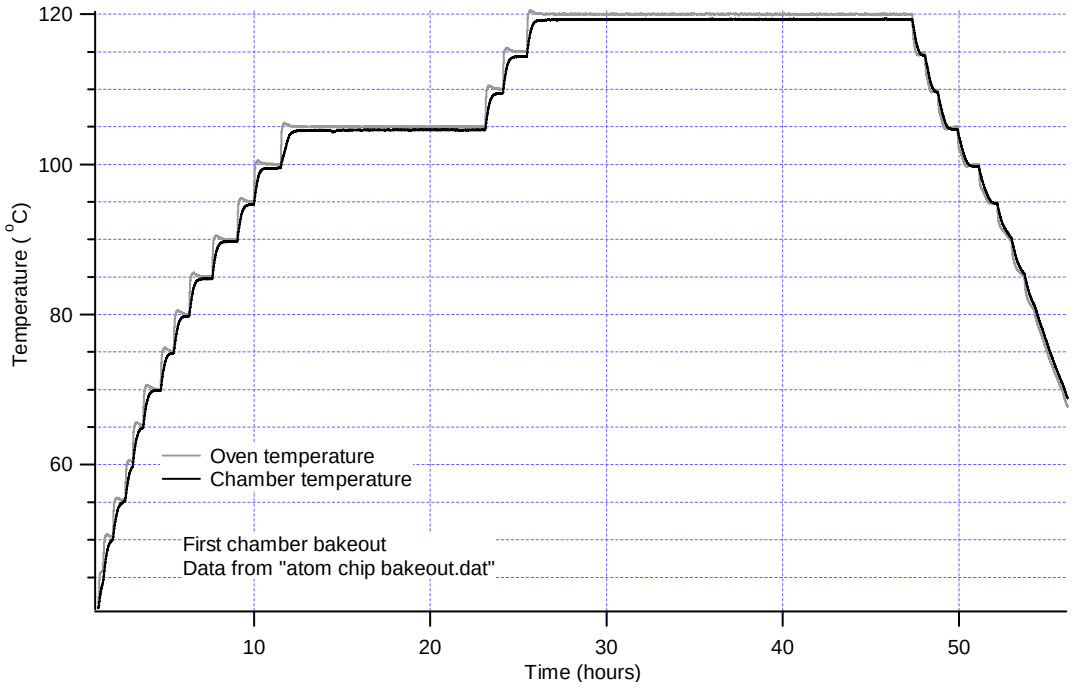

(a)

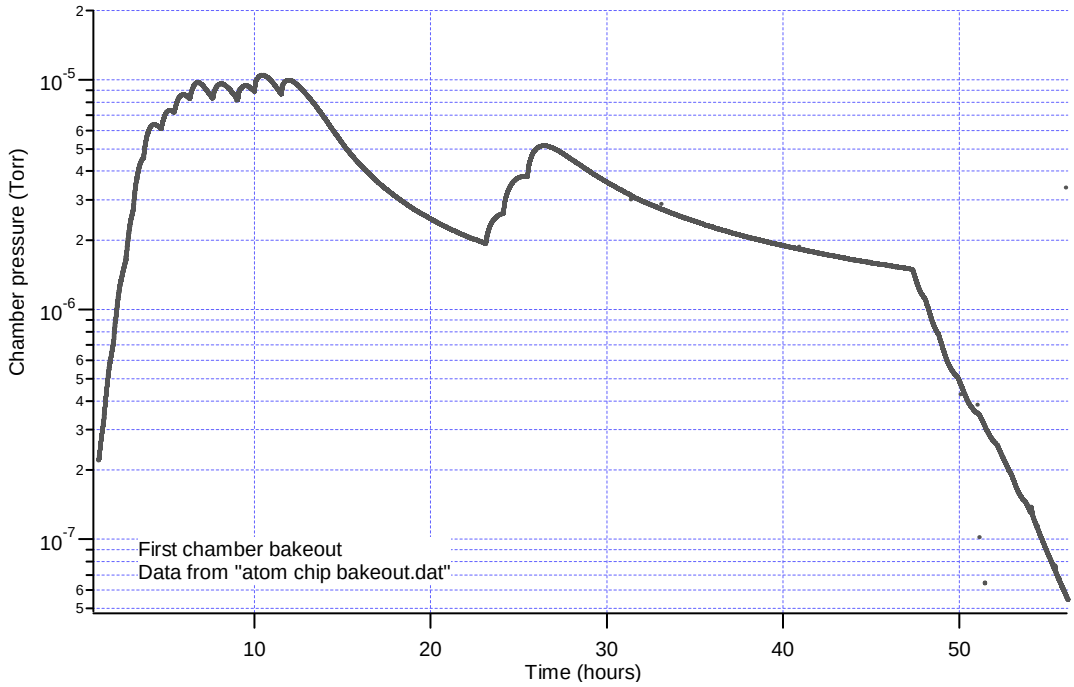

(b)

Figure 3.3: Vacuum chamber temperature (a) and pressure (b) profiles during the first bakeout cycle.

.

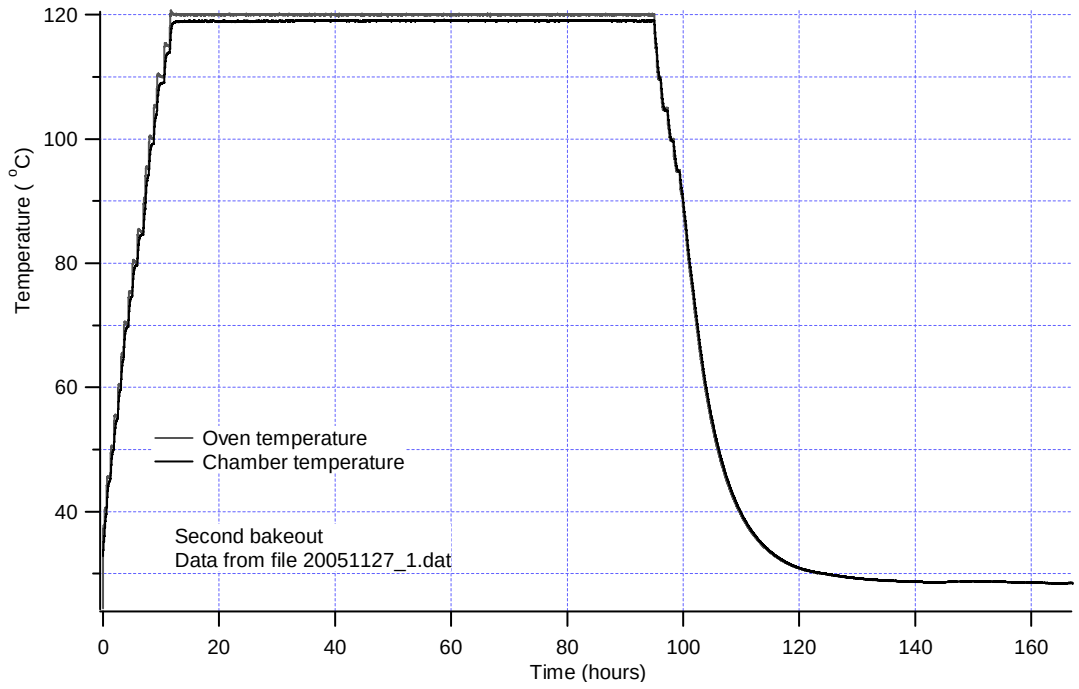

(a)

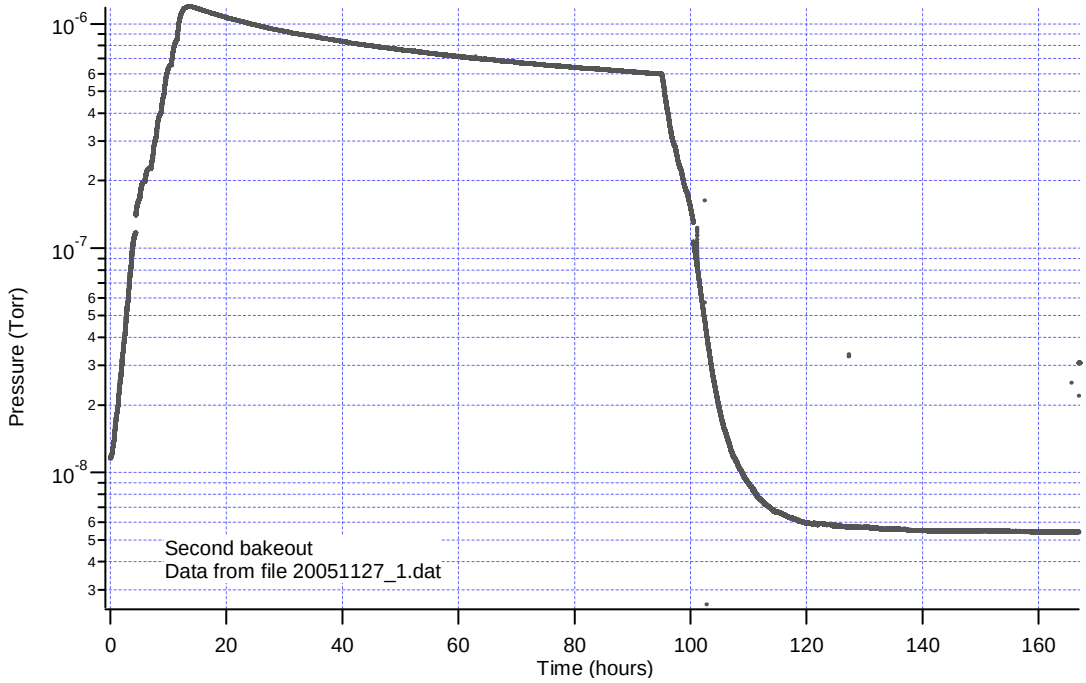

(b)

Figure 3.4: Vacuum chamber temperature (a) and pressure (b) profiles during the second bakeout cycle.

.

The background pressure will have to be lowered to increase the trap lifetime to allow for efficient evaporative cooling. More frequent operation of the titanium sublimation pump will probably help (up to the point of loading the S-trap, the background pressure has had no effect on proper operation, so it has been run very infrequently). Pulsed operation of the dispensers will raise the partial pressure of rubidium only during the MOT loading phase (the only time it is beneficial). Pulsed operation will result in lower average power dissipation, which will keep the chamber cooler and reduce hydrogen diffusion into the chamber. Using photo-desorption to increase the rubidium partial pressure during the MOT loading phase [35] would have a similar effect.

One enhancement to consider for future vacuum chambers is an adjoining differentially pumped chamber where a vapor-cell MOT is used to create a cold atomic beam, a configuration known as a low velocity intense source, or LVIS [36]. The mirror MOT near the chip is then loaded from the beam. This largely removes the trade-off between MOT loading rate and magnetic trap lifetime since the LVIS chamber can be run with a relatively high rubidium vapor pressure for an intense beam while the background pressure in the science chamber containing the chip is kept much lower. This scheme has the additional advantage of loading the science chamber with only the rubidium isotope of interest. Unfortunately, optical access constraints may preclude installation of an LVIS on the current chamber.

Organic contamination from grease or evaporating epoxy does not seem to be a problem as hydrogen very clearly dominates the mass spectra taken with the RGA (an example is given in Fig. 3.5). Reducing the hydrogen gas load in a stainless steel UHV chamber is difficult. Hydrogen is dissolved in stainless steel when it is manufactured and slowly diffuses into the chamber. To reduce the diffusion rate at room temperature, the chamber must be baked out at high temperature (400°C is

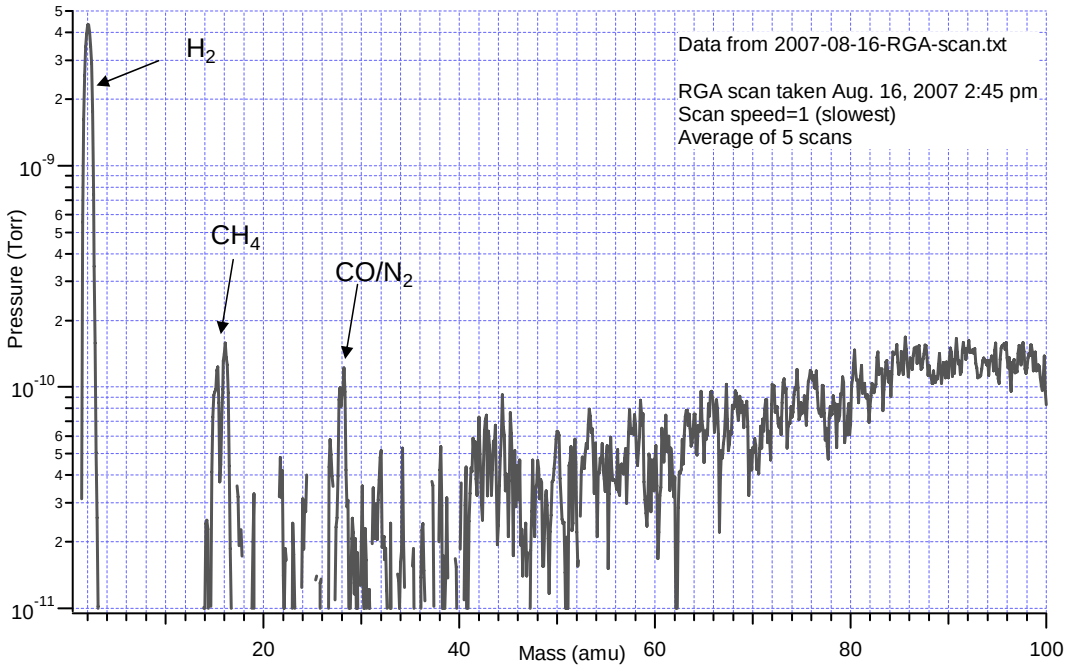

Figure 3.5: RGA scan of the background gas in the vacuum chamber. Four peaks are clearly above the noise floor, at 2 amu (H_2), 15 & 16 amu (CH_4) and 28 amu (CO or N_2). The principal peaks of CO and N_2 both lie at 28 amu, and the secondary peaks (12 and 16 amu for CO, 14 amu for N_2) are buried in the noise floor or, in the case of the 16 amu peak, buried in the CH_4 signal. The ion gauge indicated a pressure of 3.0×10^{-9} Torr during the scan, corresponding to a chamber pressure of approximately $6.5 \times 10^{-}9$ Torr $\pm 2 \times 10^{-9}$ Torr.

.

typical) so that hydrogen rapidly diffuses out of the steel and its concentration near the surface is reduced. Alternatively, the chamber walls can be cooled to cryogenic temperatures during operation to reduce the diffusion rate. Implementing either of these approaches would require substantial changes to the materials and construction of the chamber.

3.3 Magnetic Field Generation

The inhomogeneous magnetic fields required for the MOT and the macroscopic magnetic trap are generated with current-carrying structures underneath the surface of the atom chip, in combination with homogeneous magnetic fields produced by external coils in Helmholtz configuration. Reference [31] was used extensively as a guide to determine the necessary dimensions and field gradients. There are no "anti-Helmholtz" coils, which in this experimental setup would be very difficult to package around the chamber, as well as being difficult to shut off rapidly due to their relatively high inductance.

The layout of the external coils is shown in Fig. 3.6. All of them are wound with 15-gauge lacquer-coated solid copper wire on anodized aluminum frames. The coils are very tightly packaged around the vacuum chamber, and are as close to the ideal Helmholtz spacing as practical. The x- and z-coils are square rather than round so that they can fit more tightly around the chamber, while the y-coils are round to fit around the 6-inch flanges on the chamber ends. The coils have been kept as small as possible so that the inductance and power dissipation of the coils are also reasonably small. To verify the performance of the coils, the magnetic field produced at the trap center for a given coil current was measured with a Gauss meter before attaching the 6-inch flanges. Coil parameters are summarized in table 3.1. Water cooling is used to allow the coils to handle up to 15 A of current without undue heating.

Axis	Number of turns	Diameter (cm)	Ideal Spacing (cm)	Actual Spacing (cm)	Magnetic field at trap center (G/A)
x	64	22.6	12.2	12.3	4.60
y	36	17.9	9.0	9.1	3.55
z	64	29.9	16.1	14.5	3.90

Table 3.1: External coil parameters.

Underneath the chip surface are two copper conductors. These conductors were machined from OFE copper (alloy 101) for UHV compatibility and are designed to handle up to 60 A of current. These conductors are connected to the electrical feedthroughs through 1/8-inch diameter solid OFE copper conductors. The conductors are secured inside a MACOR machinable ceramic spacer with UHV-compatible epoxy (EpoTek 353ND) and electrically insulated from each other with kapton foil. The tops of the conductors were machined flat after assembly to provide a flat surface for mounting the chip. The conductors are shown in Fig. 3.8. The chip and the structure used to mount it to the 4 5/8 inch flange containing the electrical feedthroughs are shown in Fig. 3.9.

The U-shaped wire is used in combination with a bias field provided by the x- and z- coils to produce a quadrupole field for the MOT. The trapping potential is over the center section of the U, which is 14.0 mm long and has a 1 $\times$ 9 mm cross section. The leads to the center section are 3 $\times$ 3 mm. The U-wire was machined from OFE copper (alloy 101) for UHV compatibility and is designed to handle a maximum current of 60 A. The quadrupole field gradients have a much higher degree of anisotropy than a quadrupole field generated with anti-Helmholtz coils. The ratio of the field gradients (radial : radial : axial) has been calculated to be approximately 10:9:1 compared to 1:1:2 for anti-Helmholtz coils. This is actually an advantage for this experiment

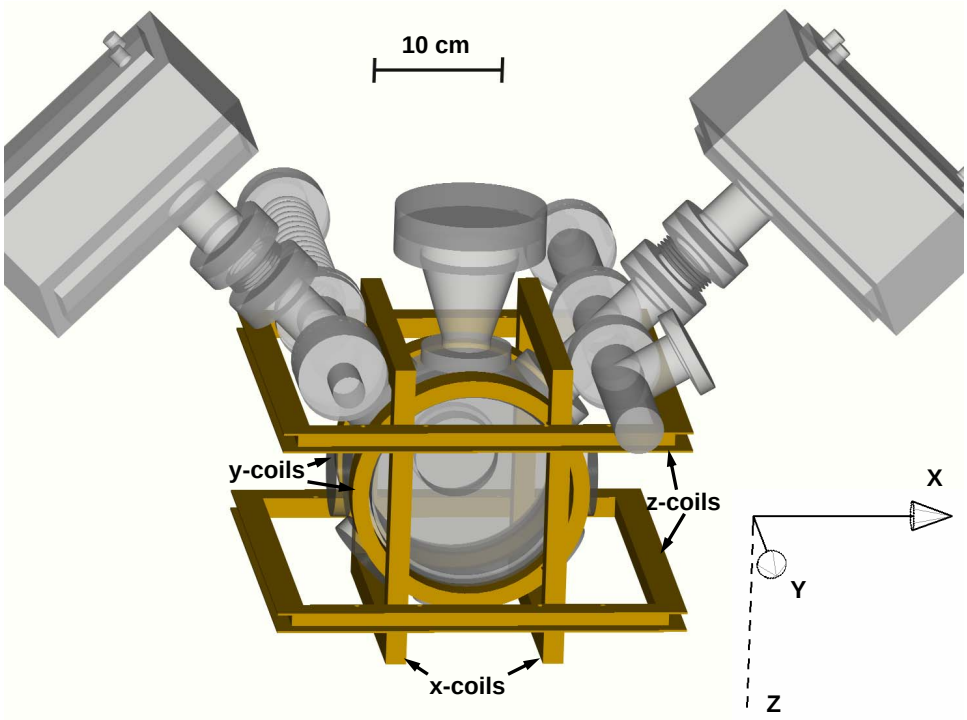

Figure 3.6: Layout of the external coils for magnetic field generation. The axes shown here reflect the convention used in all calculations, diagrams and descriptions.

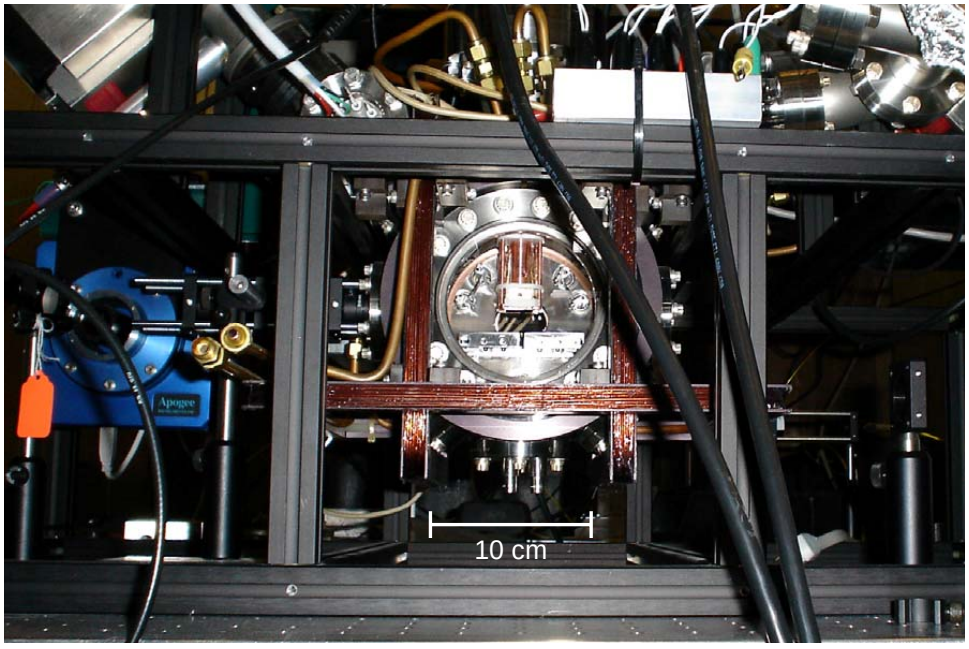

Figure 3.7: Photograph of the main chamber and external coils. The anodized aluminum frame used to support the chamber is also clearly visible.

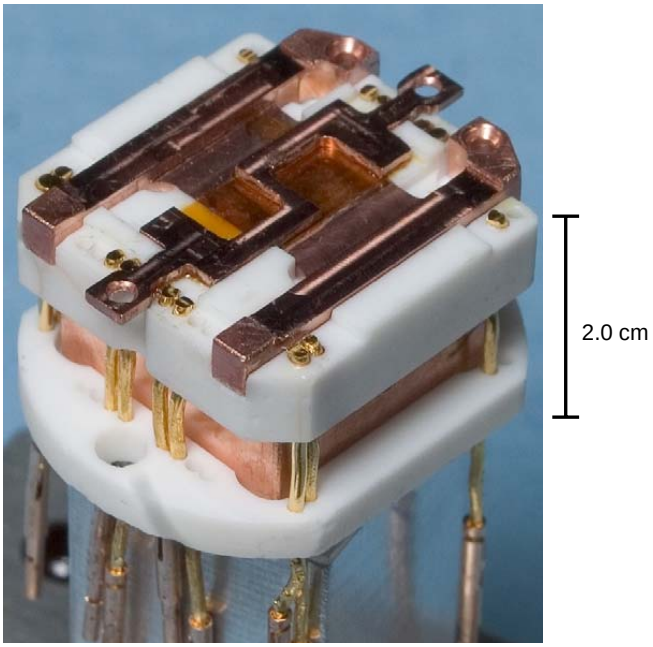

Figure 3.8: The U- and S-wires, fastened to the MACOR spacer with epoxy.

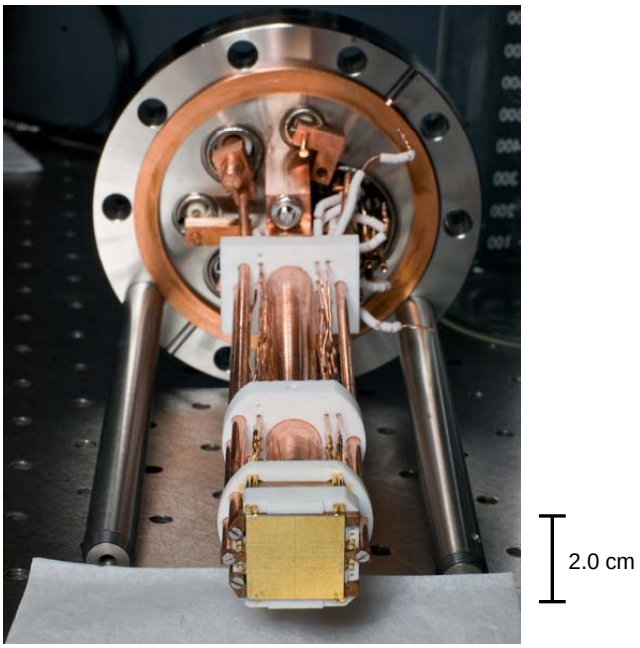

Figure 3.9: The chip and support structure, including all electrical connections, mounted on the 4 5/8 inch flange.

because the shape of the MOT cloud matches the shape of the magnetic-only traps, which are also highly anisotropic. The S-shaped wire is used in combination with the x- coils to produce a Ioffe-Pritchard trap for magnetic-only confinement. The trapping potential is generated over the center section of the S, which is 1×1 mm square and 2.8 mm long. The leads to the center section have a cross section of 2×1 mm. Depending on the desired degree of axial confinement the y-coils are also used to partially cancel the strong axial component of the magnetic field produced by the leads to the center section of the 'S'.

3.4 Atom chip

The fabrication was done by another student in the group, Owen Cherry, and is described in detail in Ref. [37]. However, the design of the wire patterns and specification of the chip performance were part of the work described in this thesis.

Magnetostatic potentials for trapping atoms are generated by running electrical current through small wires fabricated on the surface of the chip. Microfabricated gold wires on substrates have been shown to sustain current densities of up to $10^{11}\mathrm{A/m}^2$ for up to a few seconds [38]. The highest sustainable current densities are achieved for substrates with high thermal conductivity, in good thermal contact with the wires. Thus, silicon was chosen as a substrate for its high thermal conductivity and smoothness, with a very thin (40 nm) layer of SiO_2 for electrical isolation. The chip is a 2×2 cm square and is 600 μm thick.

The microfabricated gold wires are patterned using lift-off photolithography, which creates wires with much smoother edges than electroplating or etching. Roughness along the edges of the trapping wires appears to create magnetic field inhomogeneities that lead to the fragmentation of very cold clouds. The rms magnetic field spatial variation scales with distance from the chip, z, as $1/z^5$ and thus edge roughness is

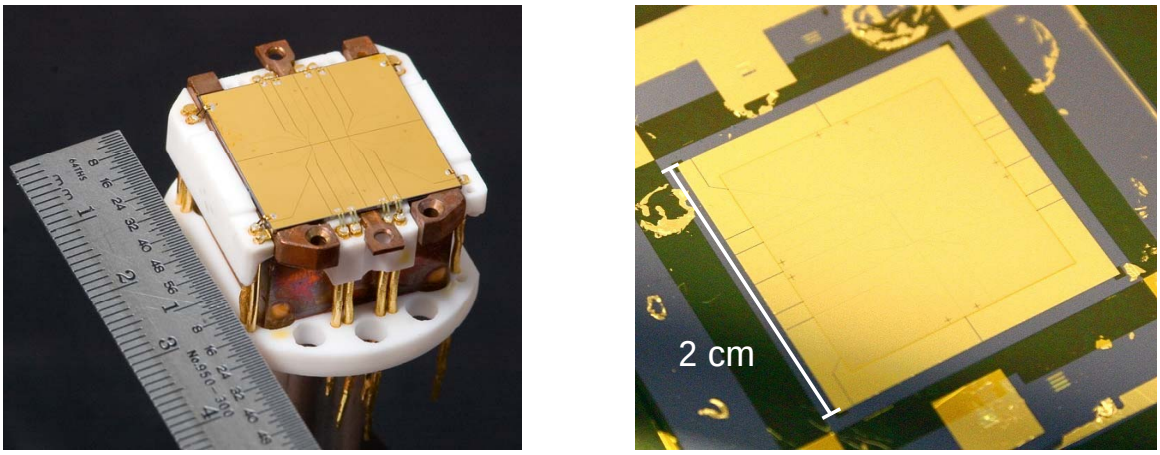

Figure 3.10: Photographs of Chip 1 (left), mounted and ready to go in the chamber and Chip 2 (right), shown before dicing to final size.

particularly troublesome when working close to the surface of the chip [39]. Lift-off photolithography also creates an optical-quality surface suitable for use in the mirror MOT. The lift-off photolithography process and use of thermal evaporation makes wires thicker than about 1 μm difficult to fabricate. The lift-off process employed also limits the feature size on the chip to approximately 5 μm or larger.

Two versions of the chip have been fabricated. Chip 1 is a single-layered device suitable for demonstrating trapping of ground state atoms and evaluating the performance of all of the experimental systems. However, the exposed dielectric gaps between wires and voltage differences between the current-carrying wires will create electric fields that will make Rydberg atom experiments difficult. Chip 2 has an additional metal electrostatic shield over the trapping wires, separated from the wires by a patterned polyimide planarizing dielectric, to provide a uniform, smooth surface suitable for Rydberg atom-surface interaction experiments. Once the chip has been diced to its final size, it is fastened to the U- and S- wires with vacuum compatible epoxy (EpoTek 353ND). Photographs of the chips are shown in Fig. 3.10.

A three-wire trap geometry was chosen for the chip. The chip design includes five parallel wires, arranged in a center H-shaped structure with two pairs of nested U-shaped wires on each side. The wire dimensions and spacing are shown in Fig. 3.11. Two different three-wire traps (the center wire and either the inner or outer pair of U-shaped wires) can be created with either chip. The inner U-wires are capable of creating a strong trapping potential in a distance range from about 2-40 μm while the outer U-wires are used to load the trap with cold atoms confined in a macroscopic magnetic trap or to perform experiments at larger distances away from the chip. The spacing of the outer U-wires was increased for Chip 2 to provide stronger confinement at large distances (50-200μm) from the chip than would be possible using the wire design of Chip 1. In both designs, the trap is 4 mm long. The radius of the cloud will range from about 1μm to at most a few tens of μm, depending on the atom-surface distance and the cloud temperature. Thus, the trap is highly anisotropic and is more appropriately considered a 2-D "guide" with sealed ends rather than a 3-D harmonic trap.

Wire currents and trap parameters at various distances from the chip surface were calculated for the Chip 1 and Chip 2 wire patterns as shown in Figs. 3.12–3.16. All distances shown are from the top surface of the wires. The calculations were performed for a 2-dimensional model, presuming that the center section is infinitely long and neglecting the contribution of the leads to the wires. For the atom-surface distances shown in the plots, this assumption is valid for all but a small region near the ends of the trap. In all cases, the wires are presumed to be 1 μm thick, and an axial field of 2 G is applied to create a harmonic potential well at the trap minimum. Current densities are presumed to be limited to 5×10^{10} A/m^2 (350 mA through the inner wires, and 700 mA through the outer wires). An illustration of the technique used to calculate the well depth is shown in Fig. 3.17.

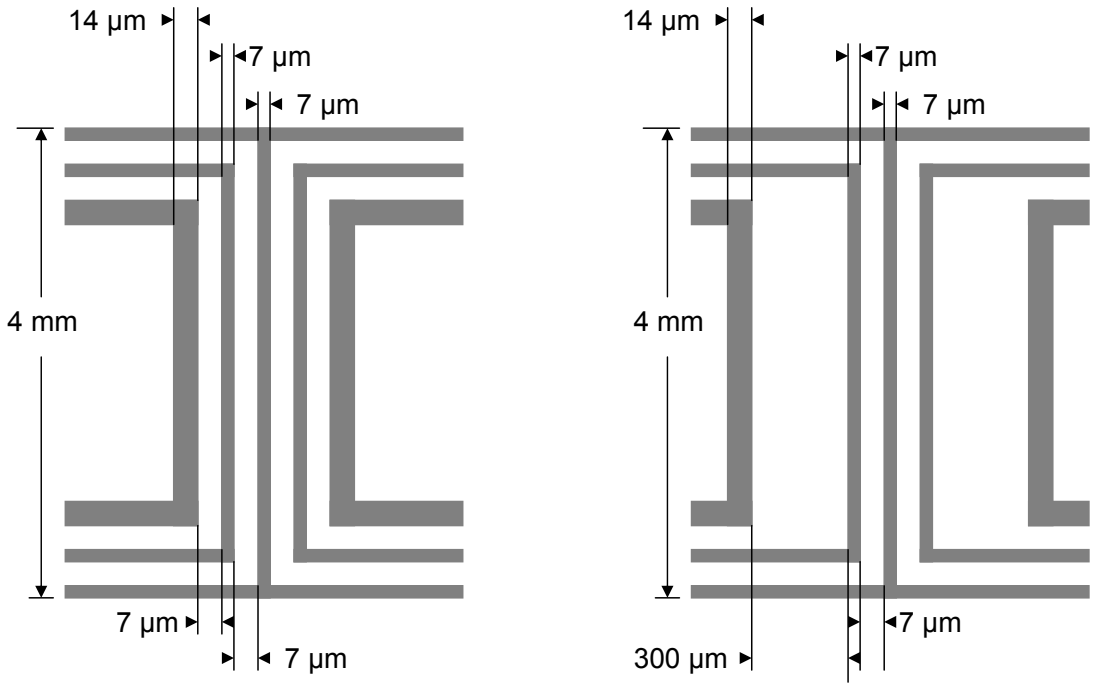

Figure 3.11: Wire schematic and dimensions for Chip 1 (left) and Chip 2 (right), showing only the center sections (not to scale).

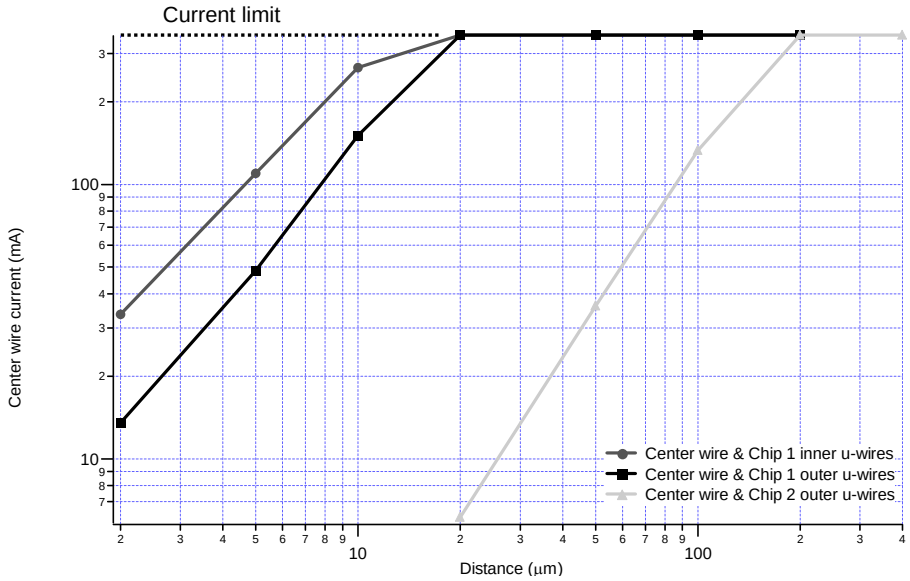

Figure 3.12: Center wire current required to form a magnetic trap at various distances from the wire surface, calculated for three different three-wire traps: The center & inner u-wires (dimensions are the same for both chip designs) as well as the center & outer wires for both chip designs.

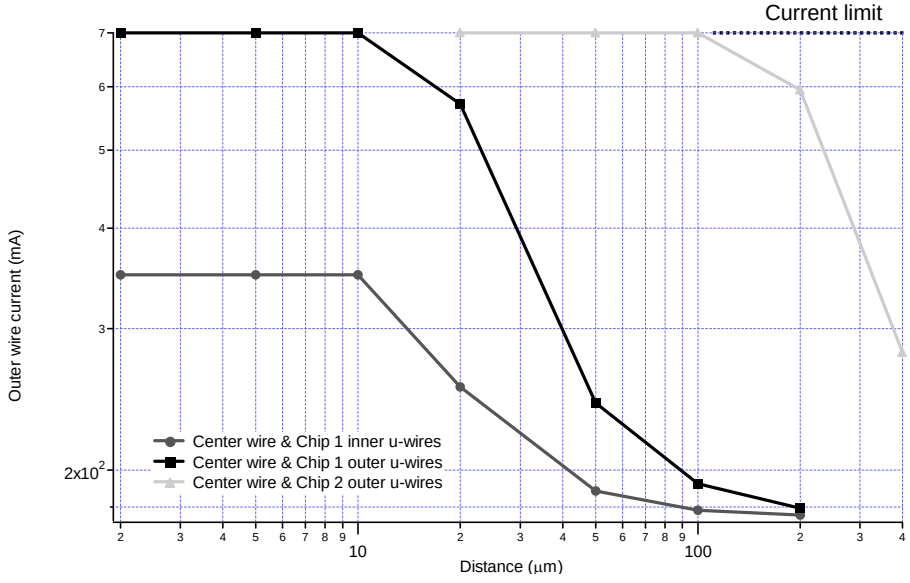

Figure 3.13: Outer wire current required to form a magnetic trap at various distances from the wire surface, calculated for same three-wire geometries as Fig. 3.12.

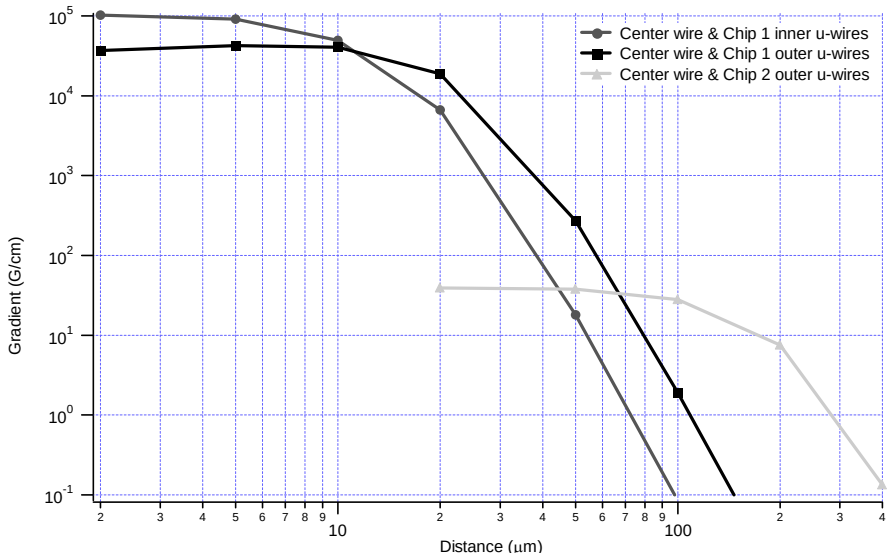

Figure 3.14: Magnetic field gradients at various distances from the wire surface, calculated for the same three-wire trap geometries as Fig. 3.12.

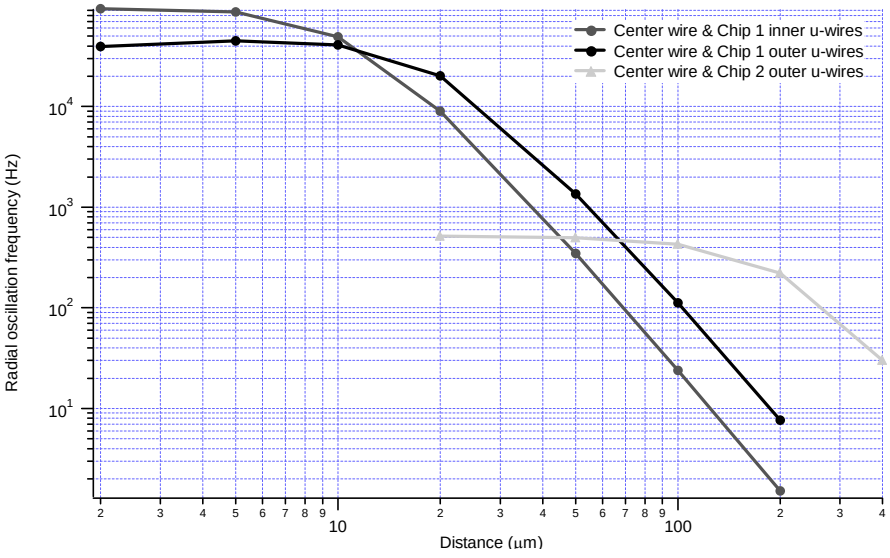

Figure 3.15: Mechanical oscillation frequency of a trapped ^{87}Rb atom in the $|F=2, m=2\rangle$ ground state at various distances from the wire surface, calculated for the same three-wire trap geometries as Fig. 3.12.

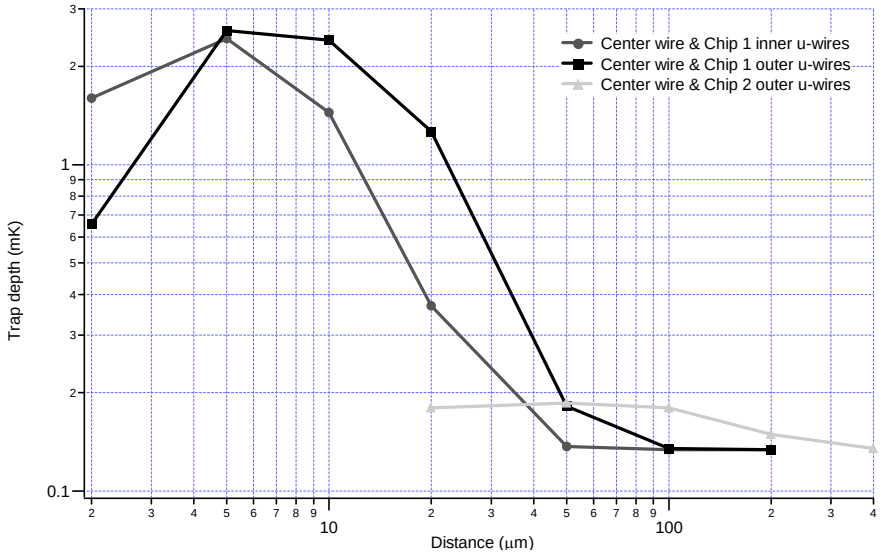

Figure 3.16: Potential well depth for a trapped ^{87}Rb atom in the |F=2, m=2> ground state at various distances from the wire surface, calculated for the same three-wire trap geometries as Fig. 3.12.

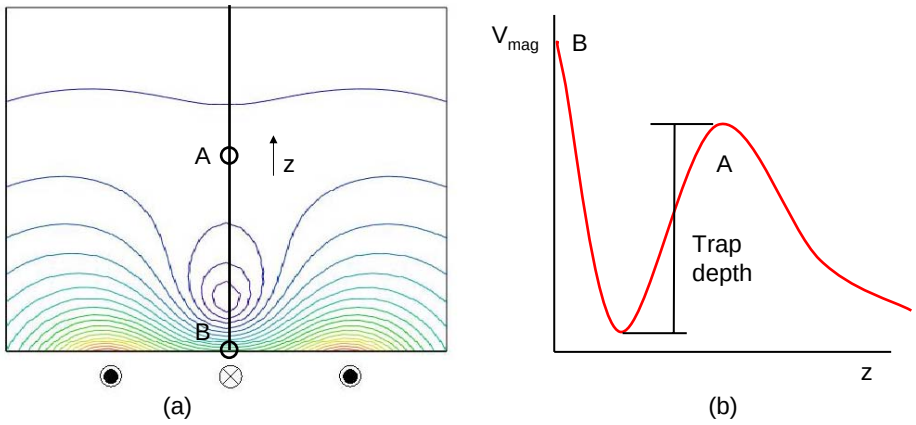

Figure 3.17: (a): Potential contours of a three-wire trap. The well depth will be limited by a saddle point above the middle wire, either at point "A" or "B" (at the chip surface).
(b): Magnetic potential along the line from "A" to "B". The magnetic potential is calculated at both locations and the lower value is taken as the trap depth.

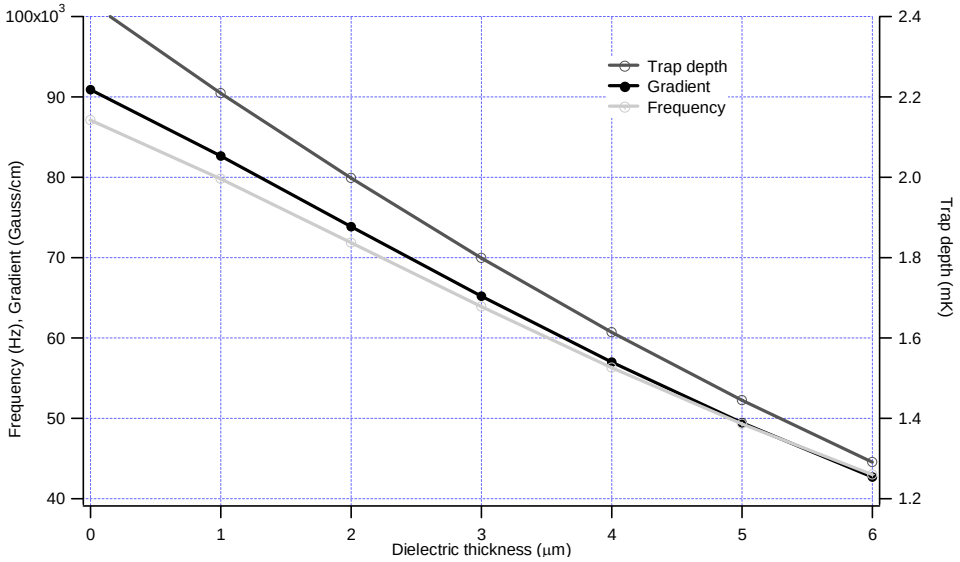

Figure 3.18: Potential well depth, magnetic field gradient and mechanical oscillation frequency of a trapped ^{87}Rb atom in the $|$F=2, m=2$>$ ground state, trapped 5 μm from the surface of a dielectric applied over the wires. The trap parameters are plotted for various thicknesses of the dielectric layer. The trapping geometry is a three-wire trap formed using the center & inner u-wires (see Fig. 3.11).

Figure 3.18 shows the effect of adding the planarizing dielectric layer, as is done in Chip 2. In all calculations for this figure, the trap was centered 5 μm above the surface of a dielectric layer above the chip wires. This calculation was done only for the three-wire trap formed using the center & inner U-wires of the chip. As the chip surface is moved away from the trapping wires, the trapping potential gets weaker for a given atom-surface distance, so a thin dielectric layer (no more than about 5μm) is desirable. As in the previous calculations, the wires are presumed to be 1 μm thick, an axial field of 2 G is applied, and the current densities are limited to 5×10^{10} A/m^2 (350 mA) through the wires.

3.5 Laser systems and frequency stabilization

3.5.1 Frequency stabilization

Three lasers are used in the ground-state atom cooling and trapping phases of the experiment. All are external-cavity CW tunable diode lasers operating at wavelengths near the ^{87}Rb D_2 line ($5^2S_{1/2} \rightarrow 5^2P_{3/2}$) at 780.241 nm. The reference laser is a low-power home-built laser, used as a stable reference for frequency control of the other lasers in the experiment. The cooling and trapping (CT) laser beam is actually split into three beamlines: most of the power goes to the cooling beams of the MOT, but it is also used for optical pumping and absorption imaging. This laser is a high-power commercial unit (Toptica DLX 110) and at 780.24 nm can produce about 350 mW of power (measured before the externally mounted isolator that is required for reliable single-mode operation). The repump laser is also a commercial unit (Toptica DL 100) with a maximum output of about 80 mW.

The reference laser is locked to the F=2→F'=3 transition using polarization spectroscopy [40]. The feedback network has two servo loops: a loop with integral gain controls the grating angle with a piezoelectric transducer (PZT) for low-bandwidth stabilization and a separate loop with proportional gain controls the diode current for faster feedback. Best results are obtained using the CW mode (100 Hz 3-dB bandwidth), rather than the high-bandwidth mode (500 kHz 3-dB bandwidth) of the controller (ILX Lightwave LDX-3525). Polarization spectroscopy was chosen as the recapture range is larger than saturated absorption. However, the frequency tends to drift through the day (the slight temperature-dependence of the zero-order wave-plates and other polarization optics is presumed to be the cause) at rates of up to 1 MHz/hour, necessitating periodic checking against a saturated absorption setup.

The CT laser is locked to the reference laser using beatnote locking [41]. Beams

from the reference and CT lasers are coincident on a single photodiode, which produces an electrical signal at the difference frequency between the two beams (in this case, about 90 MHz). An RF circuit compares the frequency of the beatnote to the frequency of a voltage-controlled oscillator (VCO) and produces a DC error signal that can be used for locking the CT laser to the reference. The frequency of the CT laser can be fine-tuned by changing the input voltage on the VCO to change its frequency.

As with the reference laser system, two servo loops are used. Again the slow loop with integral gain controls the grating angle with a PZT and the fast loop modulates the diode current. The nominal operating 'zero' frequency is defined as 80.0 MHz to the red of the F=2→F'=3 transition, so that the cooling and trapping beam (blue-shifted by this amount with a single pass through an AOM) is exactly resonant with the transition. The frequency of the laser can be quickly (over 1-2 ms) changed by up to 60 MHz without breaking lock, and observation of the error signal on an oscilloscope indicates that the tuning stabilizes within 3-4 ms. This is important since the frequency of the laser must be adjusted several times during the course of the experiment, first during the final stage of the MOT and also for the imaging and optical pumping pulses.

The repump laser is also locked to the reference laser using beatnote locking. In this case, however, the laser frequencies are approximately 6.65 GHz apart so the detector is a fast (40 ps rise time) metal-semiconductor-metal device (Hamamatsu G4176-03). The beatnote is amplified before being mixed down with a 6.800 GHz signal to produce a sideband of about 150 MHz, which is then fed into a beatnote locking scheme similar to the one employed for the CT laser. Because short-term frequency stability is not as critical for the repump as it is for the other lasers, the repump does not have a servo loop controlling the diode current but only an integral

loop controlling the grating angle with a PZT.

3.5.2 MOT beam alignment

The cooling and repump beams necessary for MOT operation are independently controlled with AOMs (IntraAction ATM 80-A2) for variable attenuation and fast switching. Shutters (Uniblitz LS2T2) ensure that no stray light from the AOMs enters the chamber during magnetic-only confinement and imaging. The cooling light is blue-shifted by its AOM, while the repump light is red-shifted. Both beams are coupled (with orthogonal linear polarizations) into one single-mode polarization-preserving optical fiber by the use of a polarizing beamsplitter. This ensures proper alignment of the repump with respect to the trap and is not much more difficult than fiber-coupling the beams into separate fibers. About 50% coupling efficiency can be achieved for both beams with reasonable ease. Typically about 80 mW of cooling beam and 20 mW of repump exit the fiber. The beam is expanded to 1.4 cm and then split into the four beams (two axial, two radial) which make up the mirror MOT. The axial beams are centered about 3-4 mm below the surface of the chip, and the radial beams are aligned so that they strike the center of the chip (which happens approximately when the radial beams are centered on both bottom mirrors) and overlap as much as possible. Alignment of the axial beams is quite tricky and can take several attempts before a satisfactory MOT is achieved.

3.5.3 Optical pumping

Following the laser cooling and trapping, as many atoms as possible must be transferred into the $|F = 2, m_F = 2>$ maximally trapped state for purely magnetic trapping. The optical pumping beam, applied along the x-direction as shown in Fig. 3.1, is resonant with the $F = 2 \rightarrow F' = 2$ transition, and is σ^+ polarized so that

$m'_F = m_F + 1$. A magnetic field is applied in the x-direction to define an axis of quantization for the atoms. The excited state can decay down to $F = 2$ via σ^+, π, or σ^- channels but with many cycling transitions each atom will decay into the $|F = 2, m_F = 2>$ state, where it will stay because it cannot absorb a σ^+ photon from this state. Because the $F' = 2$ state can occasionally decay to the $F = 1$ state, a small amount of repump beam is also put into the chamber during the optical pulse.

In zero magnetic field, the $F = 2 \rightarrow F' = 2$ transition is 266.650 MHz below the $F = 2 \rightarrow F' = 3$ transition, or 186.650 MHz below the operating frequency of the CT laser [26]. The optical pumping beam is double-passed through an 80 MHz AOM (Intra-action) to red-shift it by 160 MHz so in zero field the CT laser would have to be red-detuned by 26.65 MHz. The required detuning in the experiment is actually slightly less as the magnetic field applied to define a quantization axis tends to blue-shift the transition by a few MHz.

3.6 Imaging

3.6.1 Imaging setup

The primary camera is a 512x512 pixel CCD still camera (Apogee Alta U260) with a mechanical shutter. The CCD has 20 μm square pixels, and is just over 1 cm square in size. In between the MOT and the camera is a telescope which enlarges the image of the MOT by a factor of two, so that the CCD resolution is 10 μm and the field of view is 5 mm square. The diffraction limit of the telescope was calculated to be approximately 10 μm. The maximum achievable resolution has been estimated by focusing the telescope on the front edge of the chip (not quite a knife edge, but reasonably sharp) and fitting traces across the edge (as shown in Fig. 3.20) to the Gaussian error function. The width of the error function fit gives a reasonable

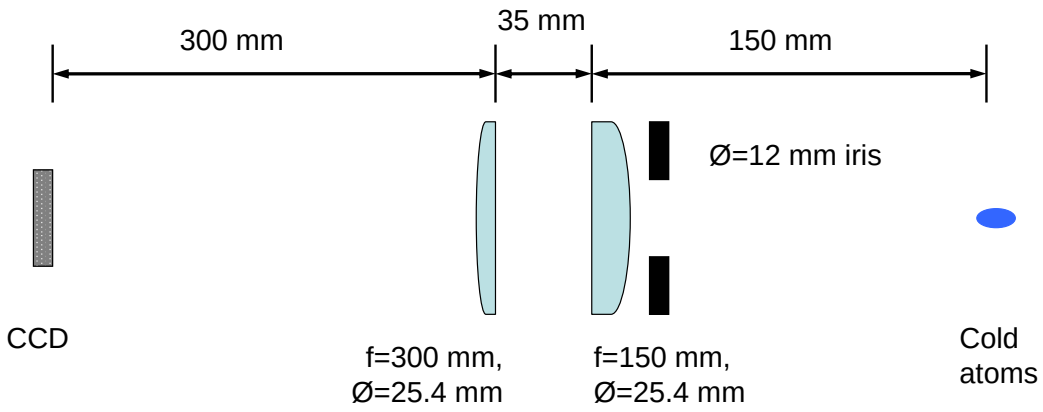

Figure 3.19: Schematic of the absorption imaging system. The iris limits the aperture of the front lens to help avoid vignetting of the image.

estimate of the imaging resolution, which is about $35 \pm 5\mu$m.

The secondary camera is a monochrome video camera (JAI CV-A50), connected to a PC with a frame grabber card (National Instruments). This camera is used to monitor the size, position and stability of the MOT cloud in real time. Software written in LabVIEW is used to calculate the number of atoms in the MOT based on the total intensity of the fluorescence viewed in the image. This PC is dedicated to controlling the video camera and monitoring the MOT population and does not control any other part of the experiment. Absolute calibration of the secondary camera has been done by focusing the fluorescence from the MOT through a lens onto a photodiode. The solid angle of fluorescence captured by the lens is calculated. Since the MOT beams are well above the saturation intensity and enough repump power is present to keep a substantial population from accumulating in the F=1 lower hyperfine ground state, each atom is presumed to scatter photons at a rate limited by the excited state lifetime, so the fluorescence per atom per unit of solid angle can be easily calculated.

The fluorescence was also measured with the primary camera, in this case calcu-

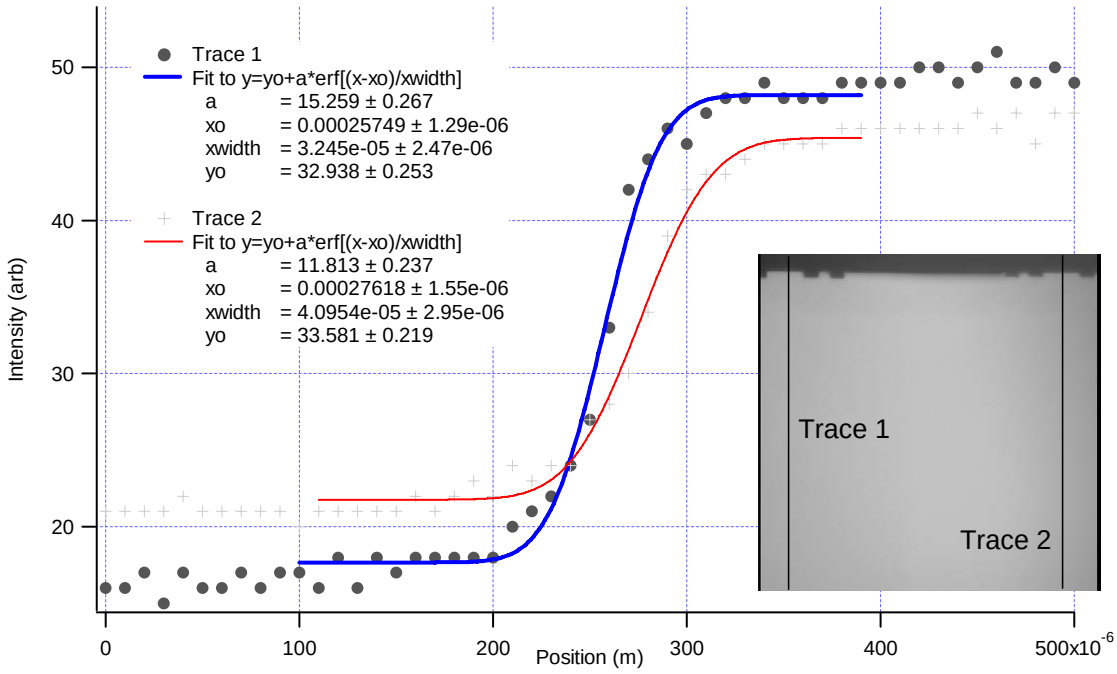

Figure 3.20: Estimation of the imaging resolution. The front edge of the chip is used as a knife-edge, and the intensity profile is fitted to a Gaussian error function. Traces across the middle are not practical as there is a screw head (visible but highly out of focus) which causes the edge to look blurry.

lating the solid angle captured by the front lens of the imaging telescope and taking into account the quoted quantum efficiency (46%) of the CCD at 780 nm. Typically the MOT number measured in this fashion is about 2/3 of the number reported by the secondary camera. The reason for this discrepancy is unclear but vignetting in the primary camera optics may be responsible.

3.6.2 Absorption imaging

The number of trapped atoms is measured with the primary camera using absorption imaging. Light from the imaging beam is directed toward the primary camera so that when atoms are present they scatter some of the beam, forming a shadow on the camera CCD. The imaging beam is resonant with the $F = 2 \rightarrow F' = 3$ transition, so that the atoms decay to the $F = 2$ ground state and each atom can scatter many photons, improving the signal-to-noise. The intensity of the imaging beam is kept well below saturation and the imaging pulse is short enough that decay to the $F = 1$ dark state does not seriously affect the accuracy of the absorption imaging measurement.

The primary camera has a mechanical shutter, which must be triggered about 13 ms prior to the imaging pulse. The shutter takes about 5 ms to completely open, so in the last 5 ms before the imaging pulse all the beams to the trap must be shut off. During this time the magnetic fields are shut off and the cloud is allowed to expand. This allows more accurate measurements of the atom number because inhomogeneous magnetic fields can shift the atoms in part of the trap out of resonance with the imaging beam. However, the cloud expands if it is not magnetically trapped. This makes imaging of relatively hot clouds (such as the first phase of the MOT), which can expand to the point of being too dilute to see, rather difficult.

The imaging procedure and conversion to atom number follows the recipe of Ref. [28]. Three images are taken: first with the imaging beam on and atoms in the trap,

then a bright field background with the imaging beam on and no atoms, and then a dark field background with the imaging beam off and no atoms. The images are taken 1.5 s apart, since the camera takes about 1 s to read out the image via USB. The optical density at each pixel, given by

$$OD = ln(\frac{I_{bright} - I_{dark}}{I_{atoms} - I_{dark}}) \tag{3.1}$$

is calculated. The absorption cross-section of each atom is [28]

$$A = (\frac{1}{2})(\frac{3\lambda^2}{2\pi})(\frac{1}{1 + 4\frac{\Delta^2}{\Gamma^2}}), \tag{3.2}$$

where λ is the wavelength of the transition, Δ is the detuning of the imaging laser from resonance, and Γ is the natural linewidth of the transition. The column density of atoms is given by OD/A, and can be summed over the extent of the image of the cloud to give a total atom number. The shot-to-shot repeatability of atom number measurements taken in this fashion is about $\pm 10\%$.

Because of the loss of phase-space density in the free expansion and the heating of the atoms by scattering photons, the absorption imaging process is destructive. A sequence of absorption images to measure temperature, for example, must be obtained by repeatedly loading the MOT and then imaging each cloud while scanning the parameter of interest.

3.7 RF evaporation

RF evaporation is performed by driving the microwave-frequency ($\approx$6.8 GHz) transition from the |F=2, m=2> state to the |F=1, m=1> state, which because of the hyperfine structure of ^{87}Rb is a strong-field seeking (anti-trapped) state. Variable-frequency microwaves are generated by mixing variable-frequency RF ($\approx$ 100 MHz)

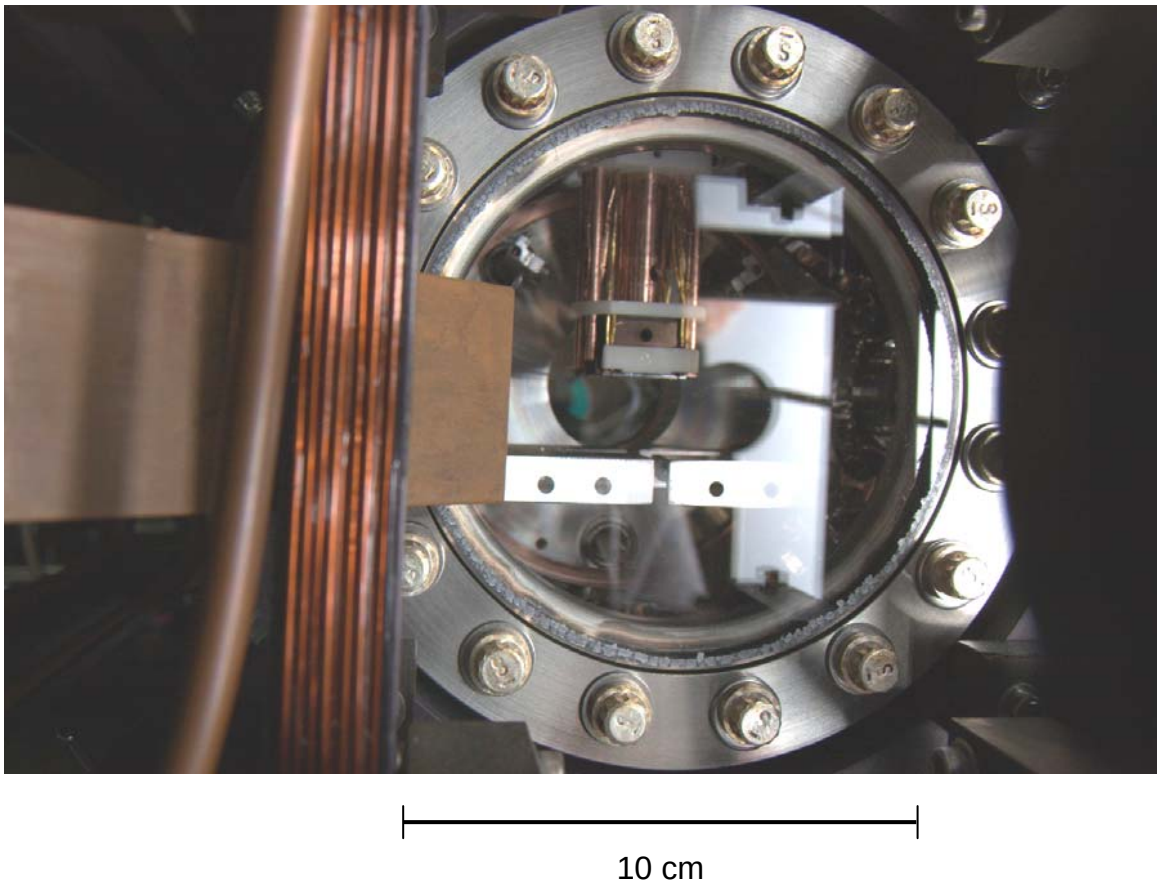

Figure 3.21: RF waveguide used to couple the 6.8 GHz microwaves into the chamber through the large window.

with a fixed-frequency microwave source. The microwaves are then amplified in a 1 watt amplifier (Minicircuits ZVE-8G) and directed toward the trap through the large 6-inch window in the vacuum chamber using a length of copper waveguide, as shown in Fig. 3.21. A microwave horn in this frequency range would be impractically large. The variable-frequency RF is produced using a signal generator mounted on a PCI card (Digital Signal Technology FSW01-PCI). The FSW01-PCI allows for full computer control of the frequency and power of the RF (over a range of about 30 dBm) and can easily be programmed to produce linear frequency sweeps.

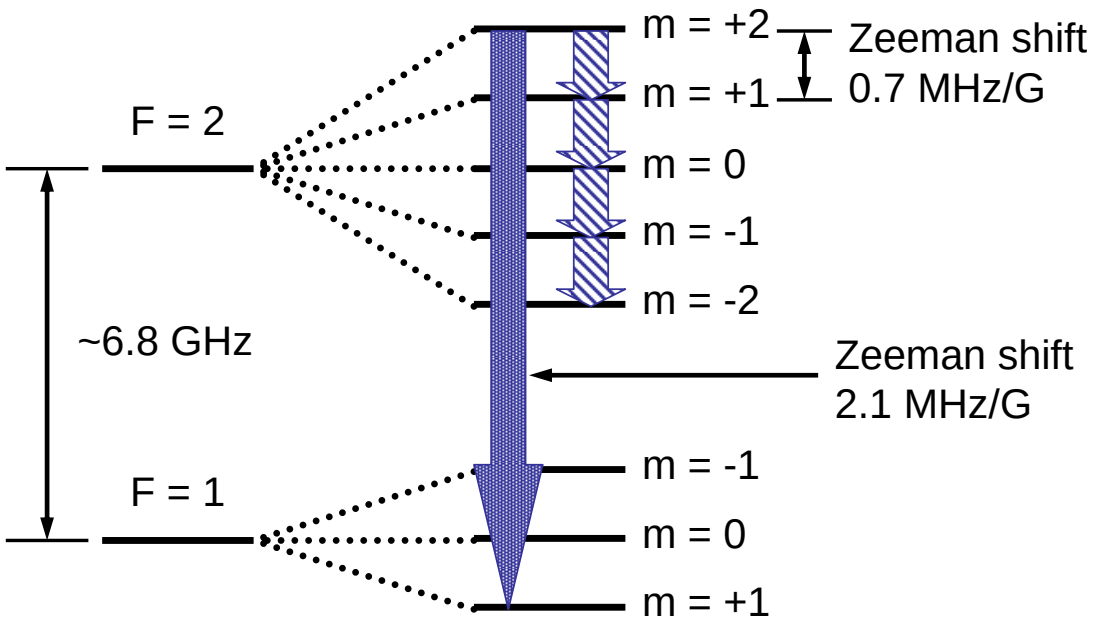

Figure 3.22: Energy levels for microwave-frequency evaporation (left), and the multi-photon RF evaporation (right) for ^{87}Rb.

The relevant energy levels of the atom are shown in Fig. 3.22. This scheme, while not novel, is not as common in the literature as is driving the atoms to the strongest anti-trapped state in the $F = 2$ upper hyperfine level, $|F = 2, m_F = -2>$, which is a four-photon process [20]. In this case, the resonant frequency depends on the magnetic field strength but is typically at most a few tens of MHz. High power, variable frequency RF at this frequency is much easier to implement than in the microwave regime. However, the frequency ramp during evaporative cooling typically spans a large fraction of the initial frequency. This can lead to the RF power present at the sample being strongly frequency dependent due to resonances in the vacuum chamber or RF generation circuit, which is a strong disadvantage of this scheme compared to microwave-frequency evaporation, where the ramp spans a much smaller range compared to the initial frequency.

3.8 Experiment Control

Fast signals are generated using a digital word generator (Interface Technologies D600, with three DG605 expansion units) connected via GPIB. The DG600 provides 224 TTL-level digital signals and can handle clock speeds of up to 50 MHz. In the current experimental configuration, the DG600 is used to provide 16 channels of fast ($< 1\mu$s settling time) analog signals through the use of 12-bit D/A converters, with an output range of -10 V to +10 V. These fast analog signals are used to control the AOM drivers as well as the current drivers for the chip wires. The remaining 32 channels, after buffering, are used as fast (100 ns resolution) digital signals. The D/A conversion electronics and digital buffers were built by the electronics shop at UW. To generate analog voltage ramps, the DG600 analog outputs can be stepped very rapidly (100 ns resolution) but this capability must be exercised cautiously as the DG600's memory depth allows only 8192 total output states during the course of the entire sequence. Therefore, executing multiple smooth ramps may yet require the addition of some simple RC filtering on some of the analog output channels.

The DG600 has a 'timing generator' mode, which allows the length of each output state to be programmed into the DG600. Unfortunately, loading commands into the DG600 when using this mode is so slow (an 8000-state sequence takes almost 30 s) that this mode is unusable for experiments. The 'word generator' mode allows for very fast loading of the command sequence (about 2 s for an 8000-state sequence). However, each state must be held for the same length of time (highly impractical) or an external trigger signal must be used as a clock signal to advance the DG600 to its next output state. The PB16 digital word generator described below was purchased primarily to provide the clock signal for the DG600.

Reconfigurable I/O devices based on field programmable gate arrays (FPGAs) have recently been developed. An example of such a device is the National Instru-

ments PCI-7811, with 160 digital channels I/O channels. In addition to controlling large numbers of digital outputs, FPGAs can be programmed to respond to external events such as trigger signals. An FPGA-based I/O board would offer much greater functionality than the DG600 and seems to be the best option for controlling large numbers of digital channels with sub-μs timing resolution.

Slow analog signals (25 μs resolution) are generated with a 32-channel (National Instruments PCI-6723) PCI analog output card. These analog outputs have a range of -10 V to +10 V, with 13-bit resolution. The PCI-6723 also has digital I/O capability, which is used to synchronize the experiment with the AC line frequency or any other desired trigger pulse. The PCI-6723 analog outputs can in principle be operated with either hardware or software triggering, but the timing resolution in the LabVIEW environment is sufficiently poor (1-2 ms) that hardware triggering is always used.

A 16-channel digital word generator PCI card (SpinCore Technologies PB16) is used to generate the clock signal for the DG600 and also provides hardware triggering for the PCI-6723. The use of the PCI-6723 to perform smooth ramps will thus be limited by the memory depth of the PB16, which is 32768 commands. The PB16 is capable of triggering with 10 ns resolution (provided each output state is held for a minimum of 90 ns) but for simplicity of programming, 100 ns resolution is used.

Some operations, such as commands to the RF generator card and downloading images from the camera, must be initiated entirely by software control and timing. Thus, the timing of these operations is accurate to only a few ms but this is not expected to be a major issue since the RF pulses and ramps will be applied on time scales ranging from hundreds of ms to a few s.

Overall control of the experiment is by a PC, using software developed with LabVIEW. The software is quite comprehensive and is used to generate and save complex sequences of control signals, perform image acquisition and analysis, and save the data

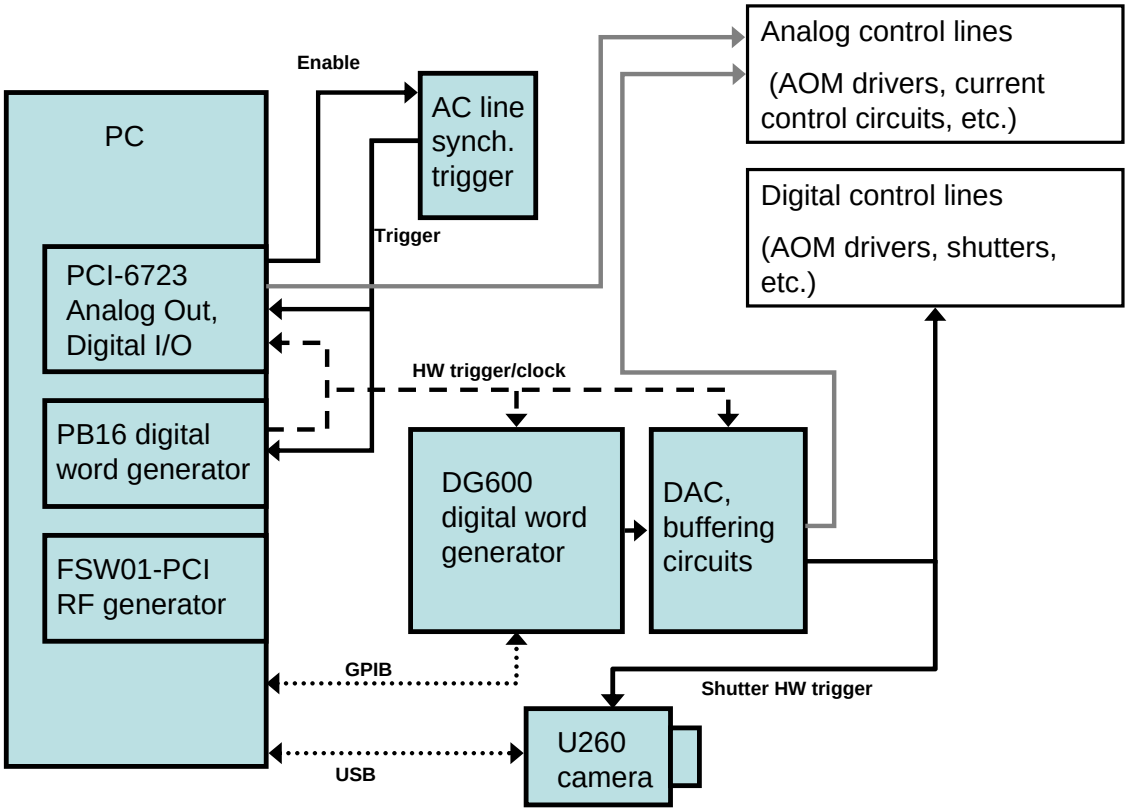

Figure 3.23: Experiment control hardware, indicating data flows, hardware timing/clock lines, and analog and digital control signals.

to file. The program can perform a series of sequences in succession, varying one or more parameters between each measurement.

Chapter 4

Characterization & Optimization

4.1 Introduction

This chapter describes the characterization and optimization of the setup. A typical experimental sequence is described, with the length of each step in the experiment. The optimal parameters for the MOT, CMOT and optical molasses phases are given. The temperature of the cloud is measured after the CMOT and optical molasses phases. The optimal parameters for the S-trap are described and the lifetime and temperature of the cloud in the S-trap are measured. Finally, the characterization of the trap with RF evaporation is described.

Frequent references to the x-, y-, and z-axes are made in the description of the experiment. The axis convention is shown in Fig. 4.1.

4.2 Experimental Sequence

A typical experimental cycle is shown in table 4.1. The whole cycle takes about 10 s, including the setup time for the digital word generators and the brightfield and darkfield background images. This is in contrast to the 10 Hz repetition rate typical

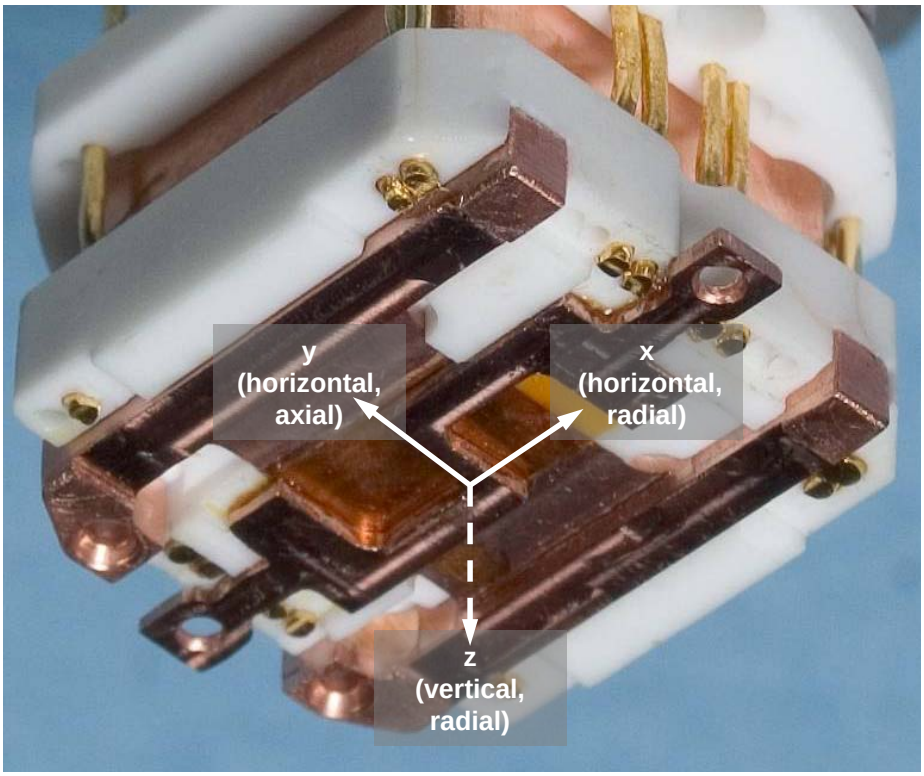

Figure 4.1: The axis convention for the experiment, shown with the U and S-wires in their proper orientation. The positive z-direction is downward, normal to the surface of the chip. The positive y-direction is parallel to the current flow in the center sections of the U and S wires, and is defined so that the current flows in the positive y-direction. The MOT and magnetically trapped clouds are cylindrically symmetric. The y-axis is the axial direction and the x- and z-axes are the radial directions.

in lab 140 [30].

In certain circumstances, multiple experimental shots within a single cycle are expected to be possible. Only a fraction of the magnetically trapped ground-state atoms will be optically excited to Rydberg states during each optical excitation pulse. If the Rydberg state transitions chosen are insensitive to magnetic fields, the experiment can be performed with the chip wire currents on, holding the remaining ground state atoms in place. Note that Rydberg excitation with the wire currents on will not be practical for Chip 1, due to the large electric fields from the exposed trapping wires.

When working with transitions sensitive to magnetic fields, the wires will have to be turned off and the ground-state atoms will fall under gravity. Thus, the trap will have to be reloaded after every Rydberg excitation. In principle, recapturing these atoms by turning on the chip wires is possible. However, a homogeneous magnetic field would have to be applied to keep the atoms in the $|F = 2, m_F = 2>$ state. Thus, this method would be impractical when studying transitions which are broadened by homogeneous magnetic fields due to Zeeman splitting. The cloud temperature would increase with each recapture, due to loss of phase-space density during the free expansion. Optimizing the recapture would likely be difficult and it seems likely to be more trouble than it would be worth.

4.3 Magneto-Optical Trap

The MOT is loaded for 6 s. During this time the cooling and repump laser beams have 80 mW and 20 mW of power, respectively. The cooling beam is detuned from the atomic transition by -13 MHz. The U-wire underneath the chip carries 36.5 A of current, and bias fields of -6.4 G in the x-direction and -1.6 G in the z-direction are applied to create a quadrupole field centered about 3 mm below the surface of

Stage	Length	Description
MOT	6 s	Load the MOT.
Ramp detuning for CMOT	10 ms	Cooling laser detuning increased.
Ramp field for CMOT	2 ms	Magnetic quadrupole zero moved toward the chip, field gradients increased.
Hold CMOT	20 ms	Cloud is compressed and cooled to 110 μK.
Ramp field for optical molasses	2 ms	Magnetic fields are ramped down to near zero.
Optical molasses	10 ms	Cooling and repump power decreased. Cloud is cooled to 40 μK.
Ramp field for optical pumping	2 ms	Magnetic field applied to define a quantization axis for optical pumping.
Optical pumping	200 μs	Optical pulse to transfer all population into $\|F = 2, m_F = 2>$ weak-field seeking state.
Ramp field for S-trap	2 ms	Ioffe-Pritchard trap loaded.
Squeeze S-trap	20 ms	Trap is compressed and moved toward the chip
RF evaporation	500 ms-2 s	Forced evaporation for cooling or diagnosing the magnetic field strength in the trap.
Future work		
Transfer to atom chip	$\approx$ 20 ms	Cloud is transferred to a trap formed by the current-carrying wires on the atom chip.
Rydberg atom experiments	$\approx$ 100 μs	Optical excitation to Rydberg states, charged-particle detection.

Table 4.1: Typical experimental sequence. Absorption imaging may be performed at any time during the sequence, but all beams must be shut off for 5 ms prior to the imaging beam pulse to allow the shutter time to open.

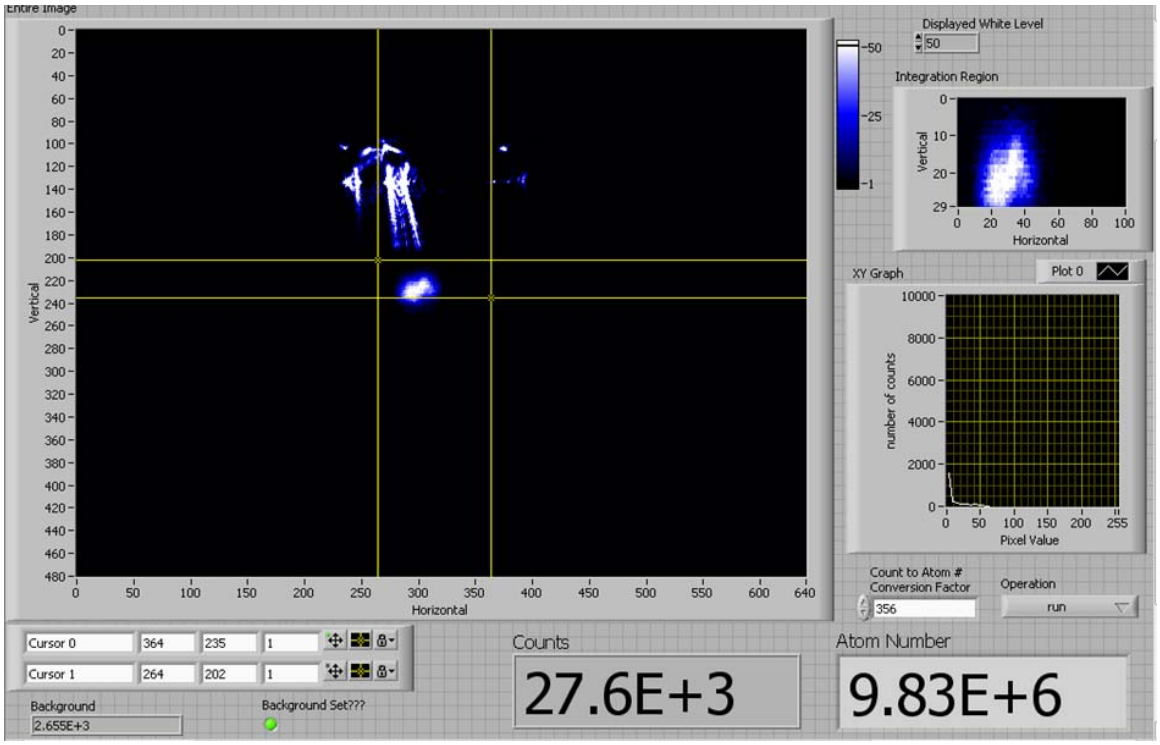

Figure 4.2: Screenshot of the program used to display MOT fluorescence imaging from the video camera and measure the number of atoms in the MOT. In this picture, the MOT cloud is about 3 mm below the chip. The light from the MOT beams scattering off the wire bonds at the edge of the chip is also clearly visible.

the chip. The MOT population tends to stabilize around $1.5 - 2.5 \times 10^7$ atoms after about 5 s (measured with the video camera/frame grabber and calibrated with the photodiode as described in section 3.6.1). A screenshot of the frame grabber program, with an image of the MOT, is shown in Fig. 4.2. The field gradient in the y-(axial) direction is small (≈ 1 G/cm) so the position of the cloud along this axis is very sensitive to the axial cooling beam balance and the magnetic field in the y-direction. In particular, the beam balance must be periodically adjusted through the day to keep the atom cloud centered over the chip.

The MOT position and intensity tend to visibly flicker in a way not seen in our similar free-space apparatus [30]. Polarization and/or intensity noise in the cooling laser were originally suspected to be the cause. However, the intensity of the MOT

beams, measured with a photodiode and a high-bandwidth amplifier, appears to be sufficiently stable to rule these out. Frequency noise in the cooling beam was also suspected, but this is also unlikely since the absorption imaging (which is much more sensitive to minor changes in laser frequency than the MOT) appears to work quite consistently. The MOT should not be very sensitive to intensity and frequency noise in the repump laser. The problem will be further investigated by comparing the bandwidths of both beatnote signals used in the cooling and repump laser locking to other setup. The stability of the reference laser will also be checked.

Other possible sources of the problem are magnetic field noise and mechanical vibration. The outputs of all the current supplies are stable, so magnetic field noise seems unlikely. Mechanical vibration is difficult to test because any impact on the chamber will affect the locking of the cooling and repump lasers, which are mounted on the same optical table.

At the end of the MOT phase, the cloud is compressed and moved toward the chip, in what is called the compressed MOT, or CMOT, phase [28]. The cooling laser detuning is ramped to -56 MHz in 10 ms. The quadrupole field is then moved toward the chip in 2 ms. The U-wire current is increased to 45.5 A, and the fields from the x, y, and z coils are changed to -12.2, 0.4, and -3.9 G, respectively. This moves the quadrupole zero to 1.3 mm away from the chip surface. The magnetic fields are held at their CMOT values for 20 ms before being ramped down in 2 ms in preparation for further cooling of the atoms with optical molasses.

The temperature of the cloud at the end of the CMOT phase was measured with ballistic expansion. Figs. 4.3 and 4.4 show the 2-D Gaussian fits after 5 ms and 13 ms, respectively. The expanded cloud fits the 2-D Gaussian quite well. Fig. 4.5 is a plot of the square of the cloud size versus the square of the expansion time. The temperature of the cloud is determined from this plot, as described in Sec. 2.5. At

the end of the CMOT phase the cloud temperature is 110 ± 10 μK.

The MOT and CMOT are both highly sensitive to the beam balance and alignment. As the MOT and the CMOT are in different locations, optimizing the beam balance for both stages at once can be quite difficult. Generally the beam balance is adjusted for optimal MOT positioning and the magnetic fields during the CMOT phase are adjusted to suppress any unwanted movement, particularly along the axial direction, while maximizing the number of atoms trapped after the end of the CMOT phase.

Optical molasses cooling [42] is done with no current through any of the coils. The optimum coil current can be determined by observing the acceleration of the cloud during the optical molasses phase. However, the optical molasses phase is so short that the small stray magnetic fields at the trap center have no appreciable effect. During optical molasses, the cooling laser detuning remains at -56 MHz. The optical molasses is applied for 11 ms and then the cooling and repump beams are turned off. The optical molasses phase reduces the temperature of the cloud to about 40 ± 5 μK, measured by ballistic expansion as described in Sec. 2.5. The plot for temperature determination is shown in Fig. 4.6.

Following the optical molasses phase, a homogeneous magnetic field of 9.2 G in the x-direction is ramped up in 2 ms to define a quantization axis for the atoms. The optical pumping beam is resonant with the $F = 2 \rightarrow F' = 2$ transition and is circularly polarized to drive σ^+ transitions to the $|F = 2, m = 2>$ state. The magnetic field lifts the degeneracy of transitions from states with different m_F, so that the cooling laser detuning required to bring the optical pumping beam into resonance with the transition ranges from 22.4 MHz to 15.9 MHz, depending on the initial m_F value. The detuning is is selected as 18.0 MHz, and the natural linewidth of the transition is sufficiently large (6.0 MHz [26]) that all of the transitions are easily excited. The

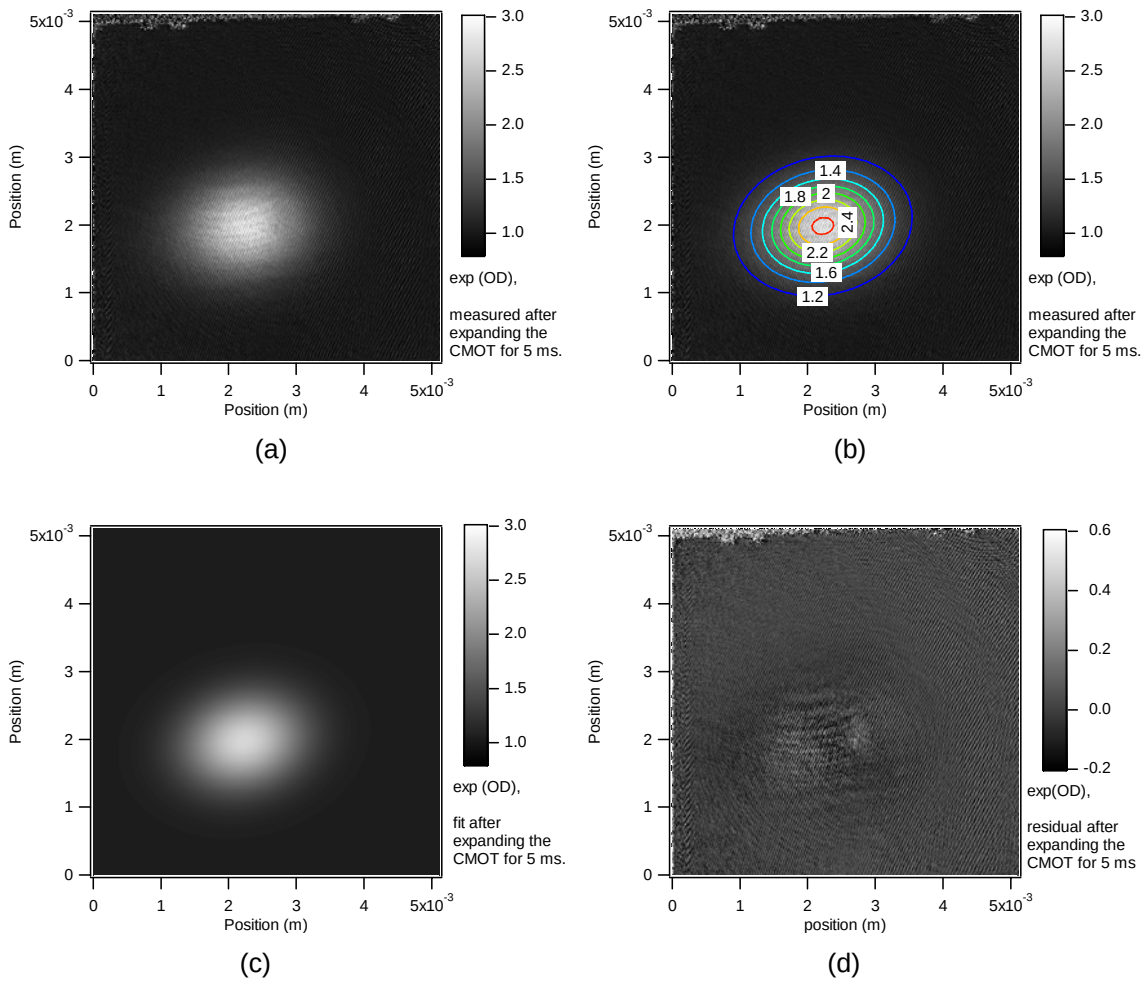

Figure 4.3: The CMOT after 5 ms of free expansion. (a): Absorption image of the CMOT. (b): Absorption image, with 2-D Gaussian fit shown in contour lines. (c): Gaussian fit to the absorption image. (d): Residual—(image)-(fit) at each point.

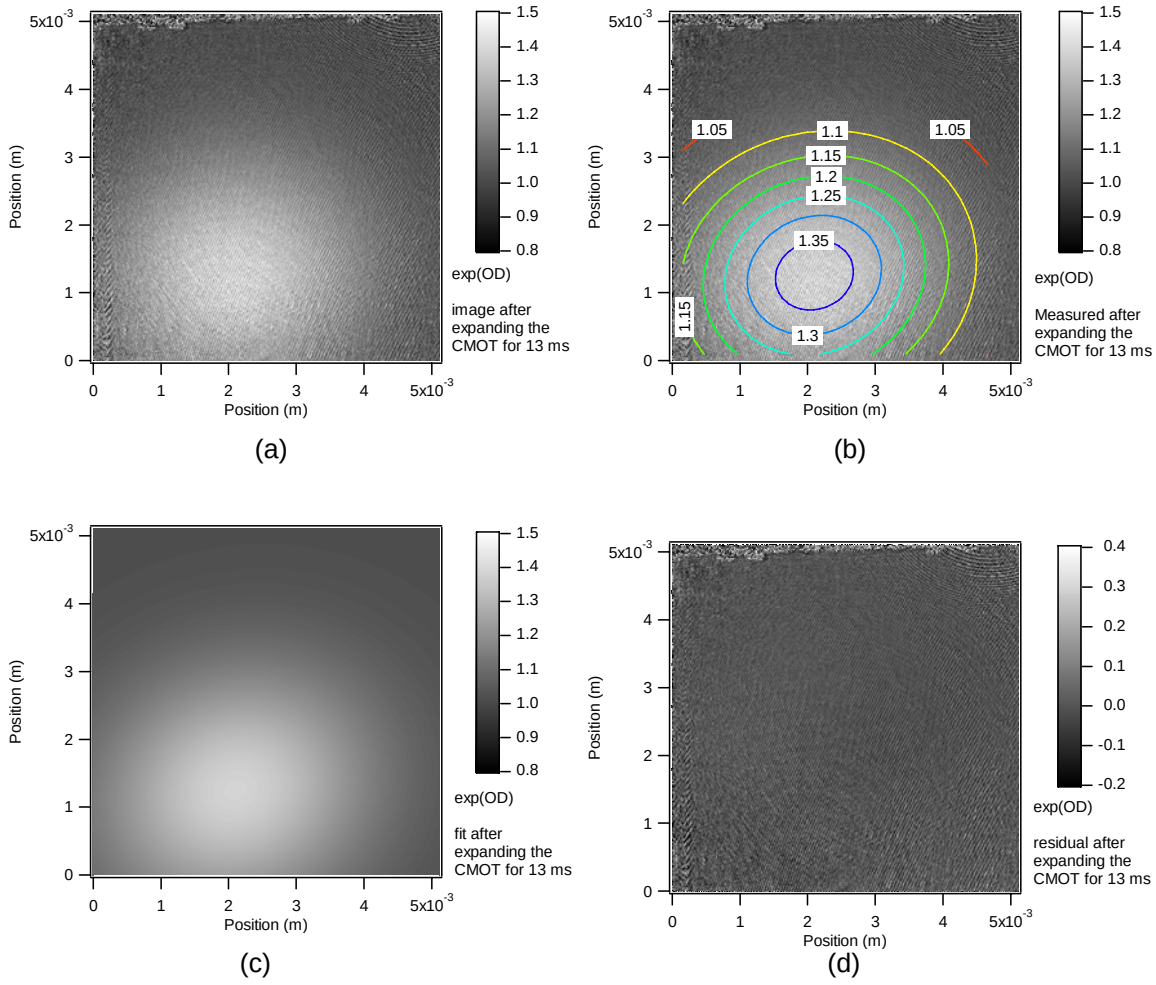

Figure 4.4: The CMOT after 5 ms of free expansion. (a): Absorption image of the CMOT. (b): Absorption image, with 2-D Gaussian fit shown in contour lines. (c): Gaussian fit to the absorption image. (d): Residual—(image)-(fit) at each point.

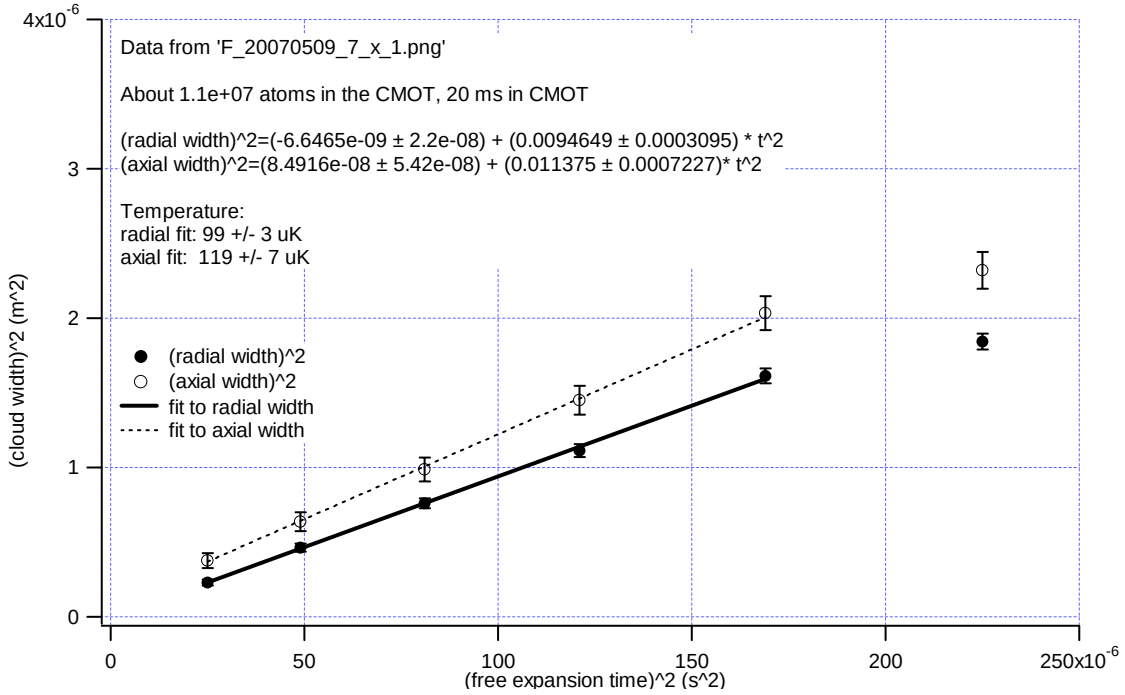

Figure 4.5: Data used to measure the temperature of the cold cloud of atoms after the CMOT phase of the experiment.

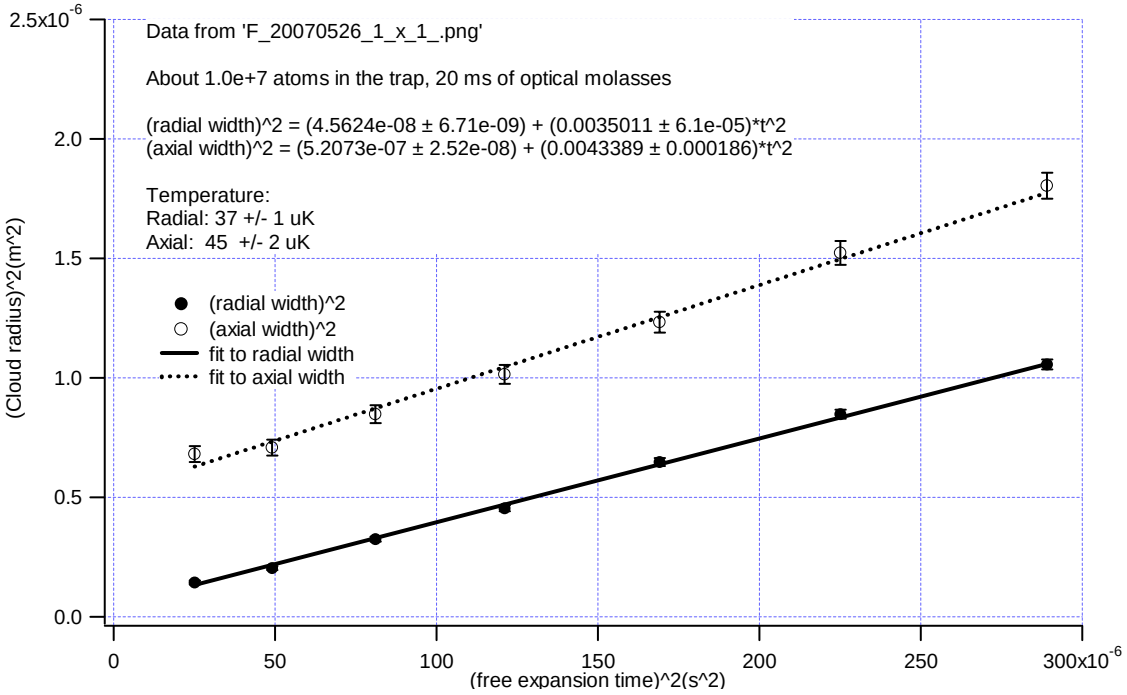

Figure 4.6: Data used to measure the temperature of the cold cloud of atoms after the optical molasses phase of the experiment.

optical pumping beam power is 200 μW, and the $1/e^2$ beam diameter is 6 mm. The beam is pulsed on for 200 μs. The repump beam must be turned on during the optical pumping pulse so that no atoms are transferred to the $F = 1$ lower hyperfine ground state. Any non-zero amount of repump power seems to be sufficient.

The population successfully loaded into the S-trap is enhanced by a factor of about five when the optical pumping pulse is applied. There are five m_F sublevels in the $F = 2$ hyperfine state, two of which ($m_F = 1$ and $m_F = 2$) are weak-field seeking. Assuming that both weak-field seeking states are trapped and all the magnetic sublevels are equally populated, the optical pumping pulse should only enhance the trapped population by a factor of 2.5. However, if only the more strongly confined $m_F = 2$ state is trapped, then the optical pumping pulse could enhance the trapped population by a factor of five as observed.

4.4 S-wire trap

Following the optical pumping pulse, the field from the x-coils is ramped up to 37 G and the current through the S-wire is ramped up to 60 A in 2 ms. Typically 70-80% of the atoms present at the end of the CMOT phase are successfully transferred to the S-wire trap. The $1/e$ lifetime of the trap is typically between 1 and 1.5 s, depending on the background pressure in the chamber. The trap lifetime tends to decrease through the day as rubidium accumulates in the chamber and the background pressure increases. The results shown in Fig. 4.7 are typical.

Images of the cloud taken after free expansion can be fit very well to a 2-D Gaussian, as shown in Figs. 4.8 and 4.9. Free expansions were done 50, 200, and 500 ms after loading the S-trap, and the temperatures determined from the plots in Figs. 4.10–4.12. The temperature of the S-trap was determined at each point. One difficulty in determining the temperature was that the atoms appear to have been accelerated

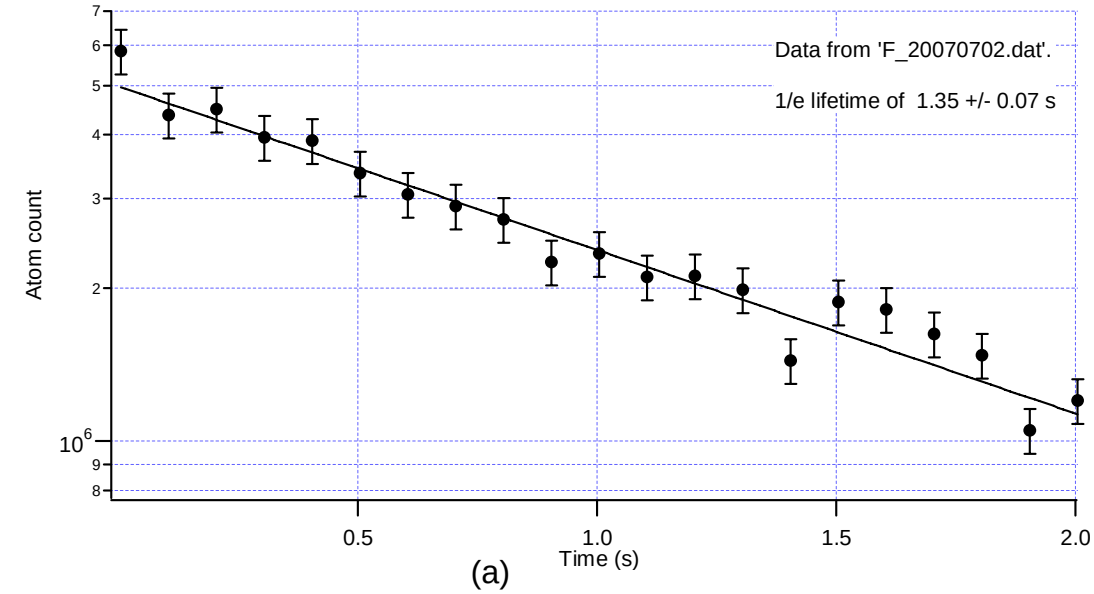

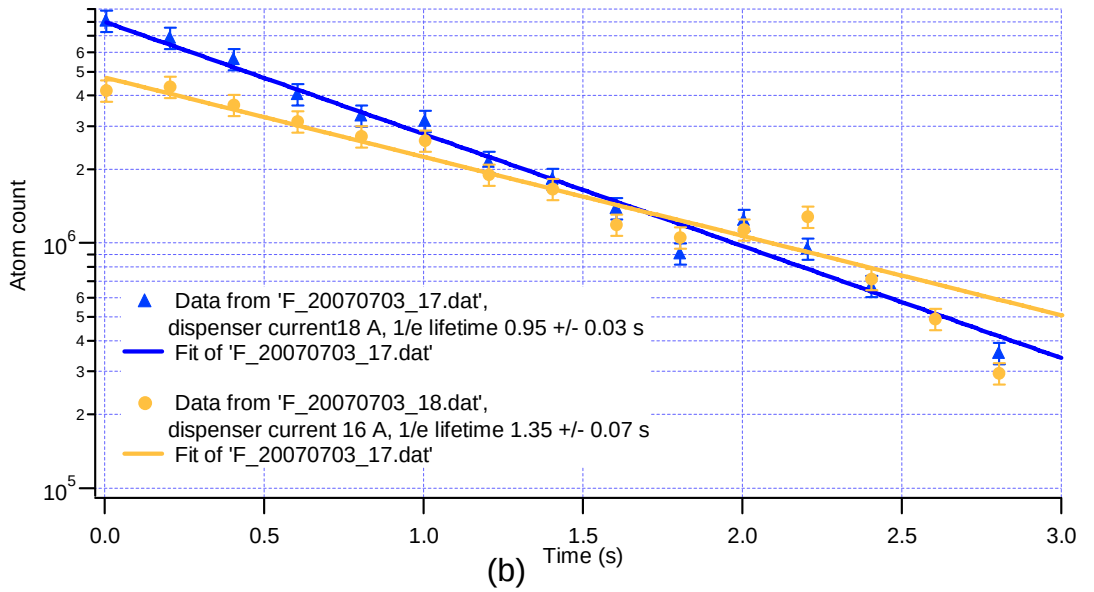

Figure 4.7: Lifetime of clouds in the S-trap. (a): Lifetime measurements taken after about 1 hour of operation. (b): Lifetime measurements taken after about 6 hours of operation. Two different dispenser current settings are shown to illustrate the tradeoff between cloud size and cloud lifetime.

in the radial direction during the ramping down of the magnetic fields. The temperature values determined by fitting the radial dimensions of the cloud were about a factor of two higher than for the axial dimensions. Acceleration of the atoms would most likely cause heating, so the lower temperature values determined by fitting the data from the axial direction are probably the most accurate. The three radial fits are quite consistent with each other, as are the three axial fits, so the temperature of the cloud in the S-trap seems to remain constant. Averaging the three axial fits, the temperature in the S-trap is approximately $42 \pm 5\mu$K.

Collisions with background gas appear to be the dominant trap loss mechanism. A lifetime of 1 s corresponds to a room-temperature hydrogen background of 2×10^{-8} Torr [21]. This is about a factor of two higher than the pressure measured with the ion gauge during experiments, but this is reasonable consistency considering the uncertainty of the ion gauge measurement. Trap loss mechanisms which would also cause heating (such as low-frequency magnetic field noise accelerating and heating the atoms) must be insignificant because very little heating was observed. Majorana transitions to untrapped states are not a likely source of trap loss for the experimental conditions of Figs. 4.10–4.12, because the magnetic field at the trap minimum was about 20 G during these measurements. The depth of the potential well is about 1 mK, so evaporation of the atoms will be quite slow.

Following the loading of the cloud into the S-trap, the trap is compressed. The field from the x-coils is increased to 46 G to compress the trap and move it closer to the chip. Next, the y-coils are used to partially offset the axial field created by the S-wire. This lowers the field at the trap minimum and compresses the trap. The applied field is typically 14 G, which makes the total field at the trap minimum about 6 G. Ballistic expansion is not practical from the compressed configuration since much of the cloud will hit the chip. The trap must first be moved away from the chip by

returning the x-coils and y-coils to the parameters used when loading the trap, and then the cloud can be expanded and imaged.

Imaging the S-trap cloud directly is useful at this stage for determining its distance from the chip. However, the inhomogeneous magnetic field will cause Zeeman shifting. Some of the atoms will be shifted out of resonance with the imaging beam, so that direct in-trap imaging will systematically undercount the total number of atoms in the trap.

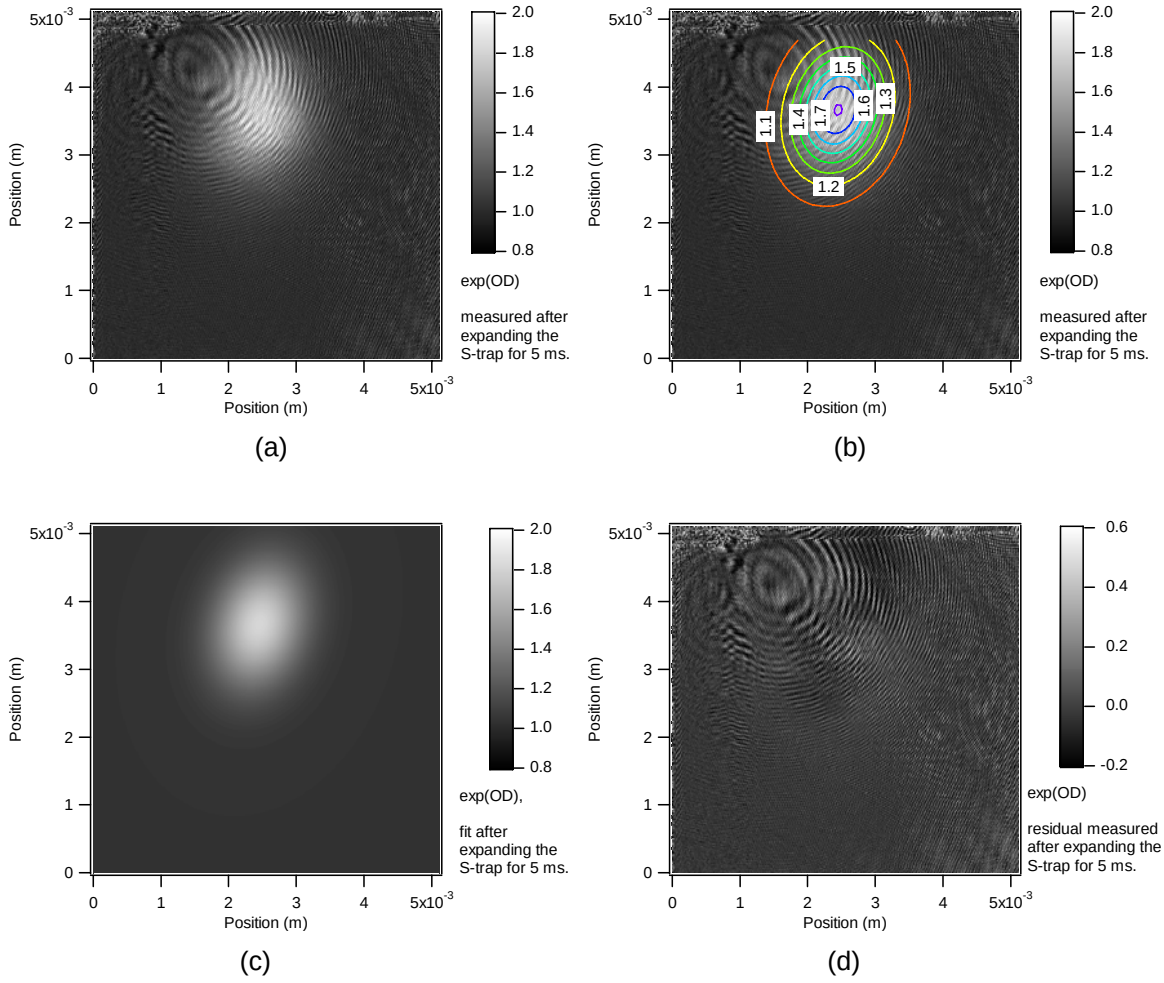

Figure 4.8: The S-trap after 200 ms of confinement and 5 ms of free expansion. (a): Absorption image of the S-trap. (b): Absorption image, with 2-D Gaussian fit shown in contour lines. (c): Gaussian fit to the absorption image. (d): Residual—(image)-(fit) at each point.

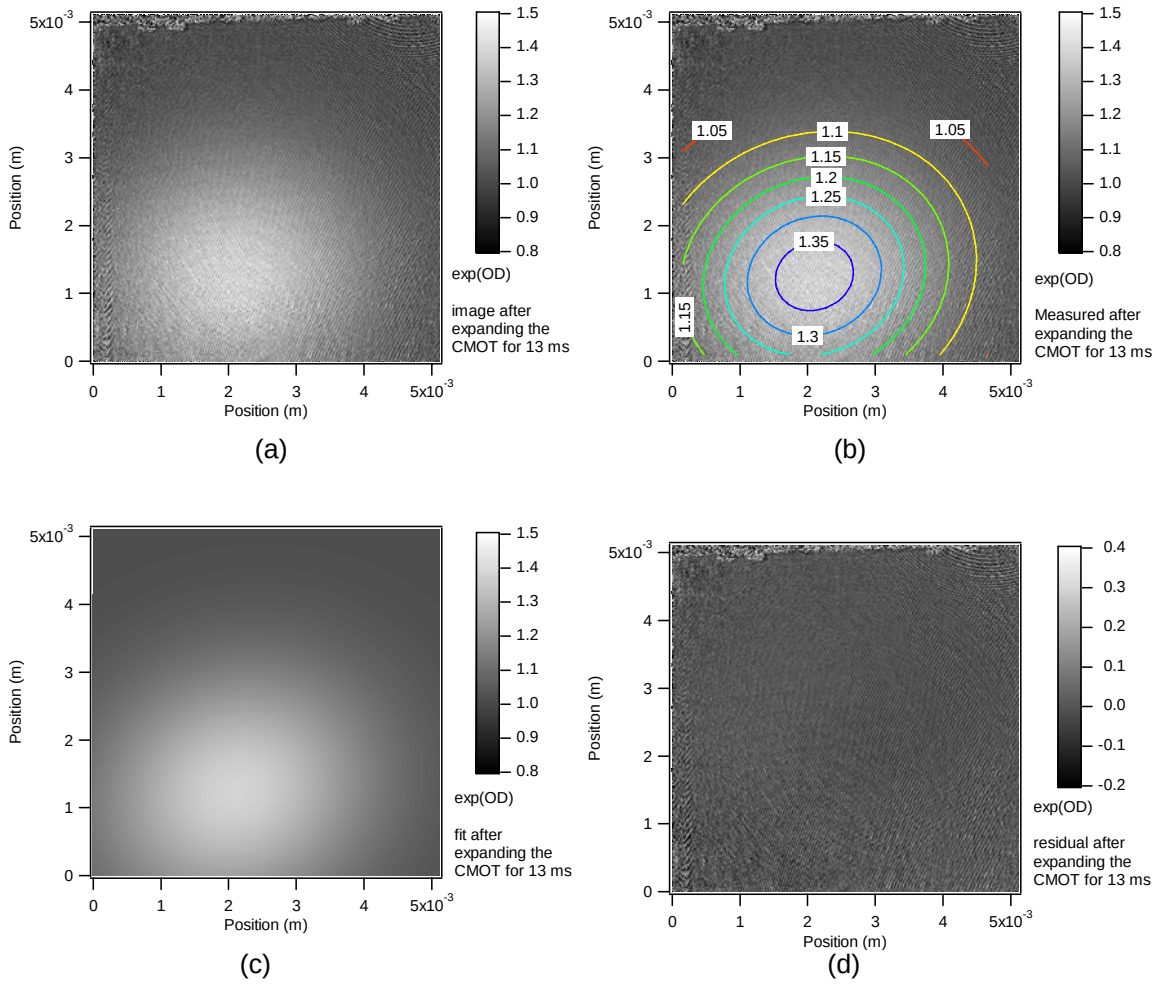

Figure 4.9: The S-trap after 200 ms of confinement and 13 ms of free expansion. (a): absorption image of the S-trap. (b): absorption image, with 2-D Gaussian fit shown in contour lines. (c): Gaussian fit to the absorption image. (d): residual—(image)-(fit) at each point.

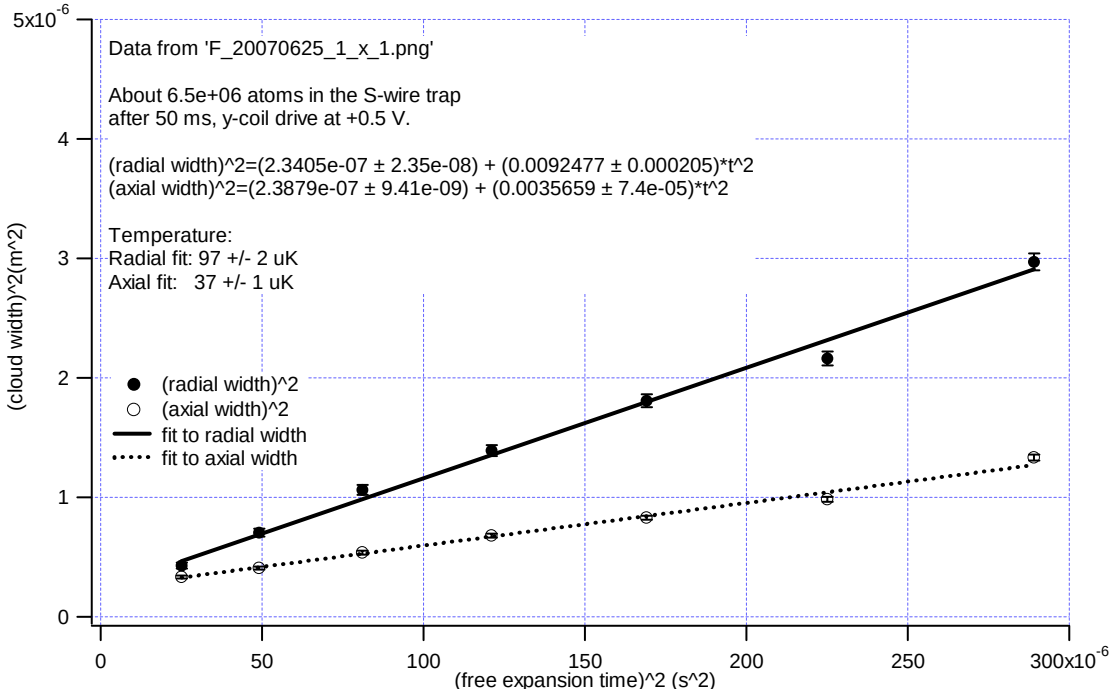

Figure 4.10: Data used to measure the temperature of the cold cloud of atoms after 50 ms of confinement in the S-trap.

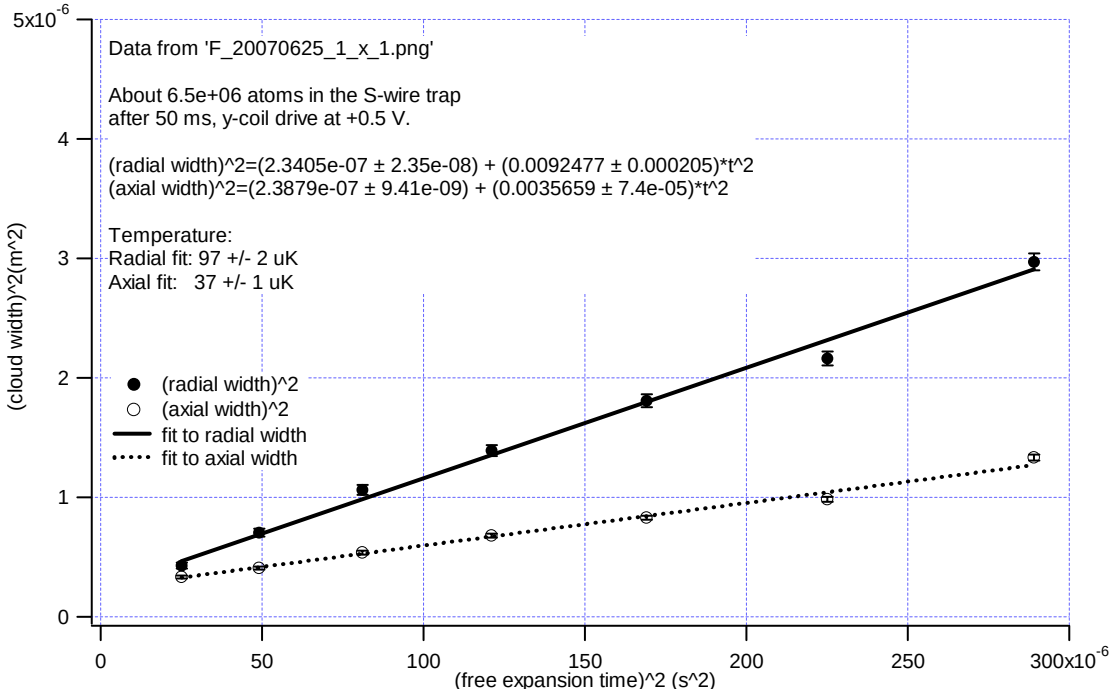

Figure 4.11: Data used to measure the temperature of the cold cloud of atoms after 200 ms of confinement in the S-trap.

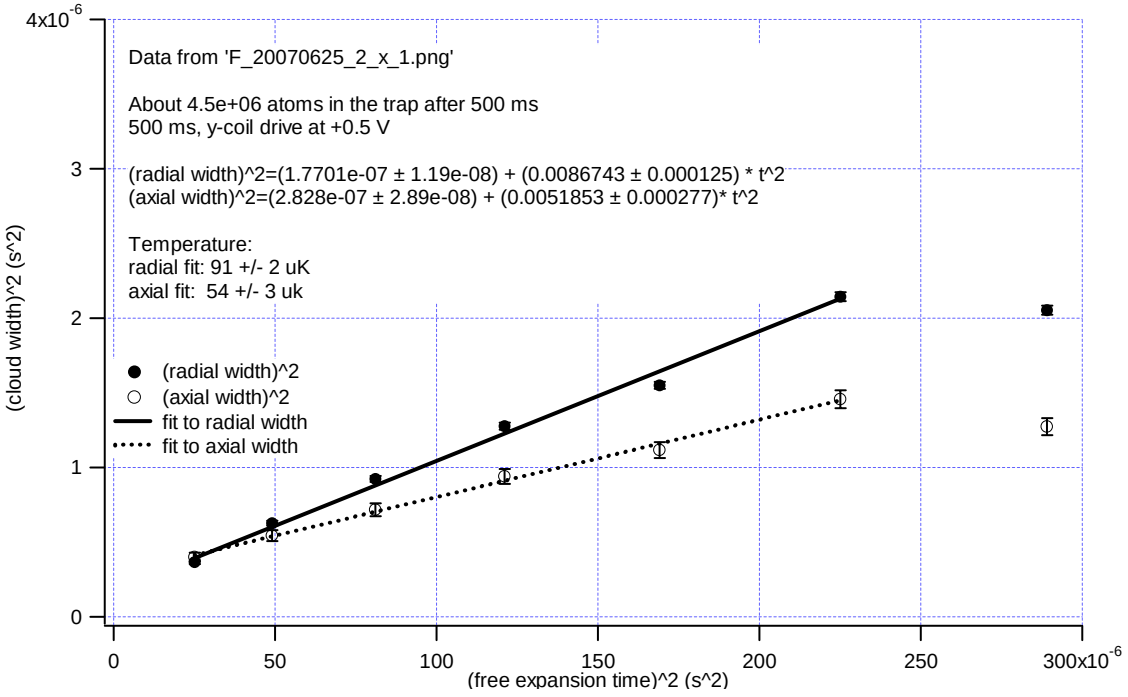

Figure 4.12: Data used to measure the temperature of the cold cloud of atoms after 500 ms of confinement in the S-trap.

4.5 RF evaporation

Following compression of the trap, RF is applied, with the goal of cooling the cloud by selectively ejecting only the hottest atoms. The RF drives a transition from the $|F = 2, m = 2>$ to the strong-field seeking $|F = 1, m = 1>$ ground state, as shown in Fig. 3.22. This transition is 6.834682 GHz in zero field, and is Zeeman shifted by +2.1 MHz/G [26]. RF evaporative cooling has not yet been demonstrated. However, RF evaporation with fixed-frequency pulses has been used to measure the magnetic field at the trap minimum. In Fig. 4.13, the onset of RF evaporation at 6.840, 6.856, and 6.878 GHz corresponds to fields at the trap minimum of 3.0, 10.5, and 21.0 G, respectively. The spectrum broadens as the trap is compressed, which is consistent with the cloud heating as it is compressed. Due to the length of the RF pulse, the atoms will oscillate through the trap repeatedly, making direct relation of the spectrum to temperature difficult.

As the data in Fig. 4.13 show, a 0.5 s long RF pulse at full power leaves a substantial fraction of the atoms remaining in the trap. This situation will have to be improved for efficient evaporative cooling. In runaway evaporative cooling, the trap population is reduced by a factor of 100–1000 [20]. Given the rate of background collisions in the vacuum chamber this will have to be done in a period of several seconds. Improving the evaporation rate will have the benefit of allowing more direct relation of the RF evaporation spectrum to the cloud temperature.

One possibility is that the remaining population is actually in the $F = 2, m_F = 1$ state and is not resonant with the RF. This can be checked by detailed study of the population in the trap as a function of the RF pulse length. If the population asymptotically approaches a non-zero value with longer RF pulses (up to 1 s will be practical given the current loss rate), the remaining population is likely in the $F = 2, m_F = 1$ state.

Another possibility is that the RF power present at the atoms is insufficient to drive the transition. The waveguide antenna should couple the RF to the atoms with reasonable efficiency. However, the intensity of the RF at the cloud has not been measured to confirm this. Releasing the cloud and attempting to drive Rabi oscillations between the $|F = 2, m_f = 2>$ and $|F = 1, m_f = 1>$ states would provide some information about the RF strength at the ground state atoms.

As the population of the atoms decreases during RF evaporation, imaging after expansion may become impractical if the cloud is too spread-out to see following the expansion. In-trap imaging (see Fig. 4.14) can be used to optimize the RF evaporation profile. In-trap imaging will be practical because the spatial extent of the cloud will decrease as it cools. Hence, the magnetic field will become more uniform over the size of the cloud so that Zeeman shifting of atoms out of resonance with the imaging beam will not be a problem.

Following the evaporative cooling stage, the atoms will be transferred from the S-trap to the chip by ramping up the currents on the chip wires while ramping down the current through the S-wire.

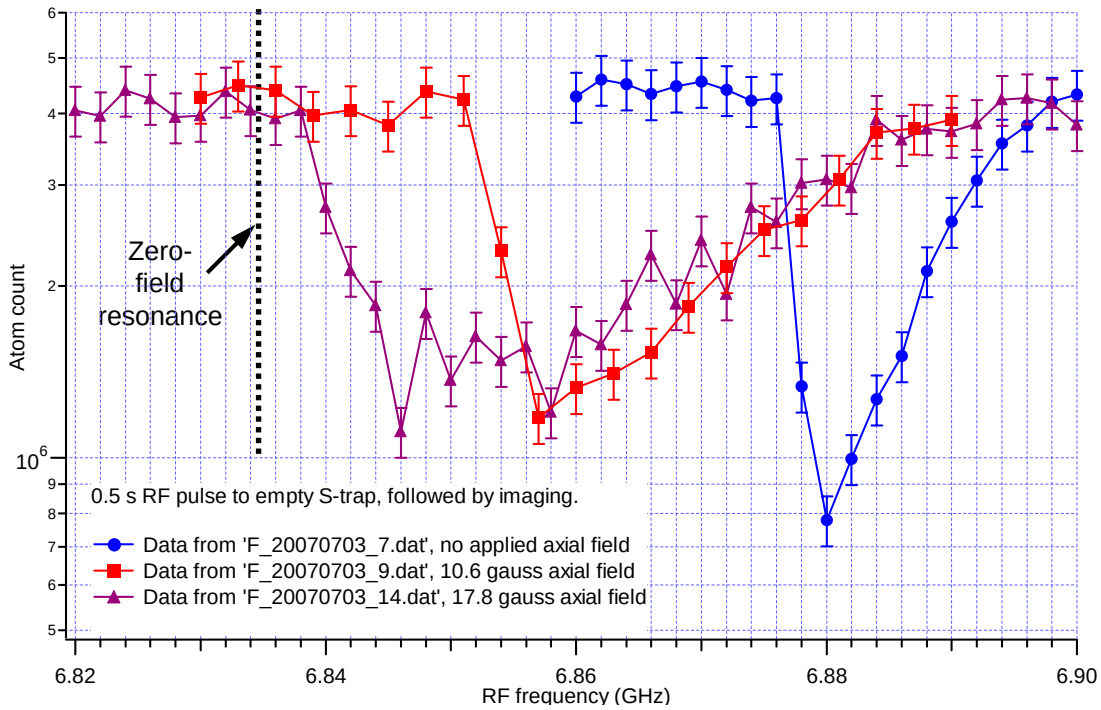

Figure 4.13: RF evaporation with a fixed-frequency pulse, 0.5 s long. The population after the pulse is measured as a function of the RF frequency generated by the RF card, which is mixed with 6.8 GHz microwaves. The resonant frequency depends on the magnetic field in the trap, and the zero-field resonance occurs at 34 MHz on this scale.

Plots are shown for three different applied axial fields, which partially cancel the field from the S-wire and compress the trap. Evaporation starts to occur at lower RF frequencies as a result. The broadening of the spectrum in the compressed traps may be attributed to the increased temperature following the compression.

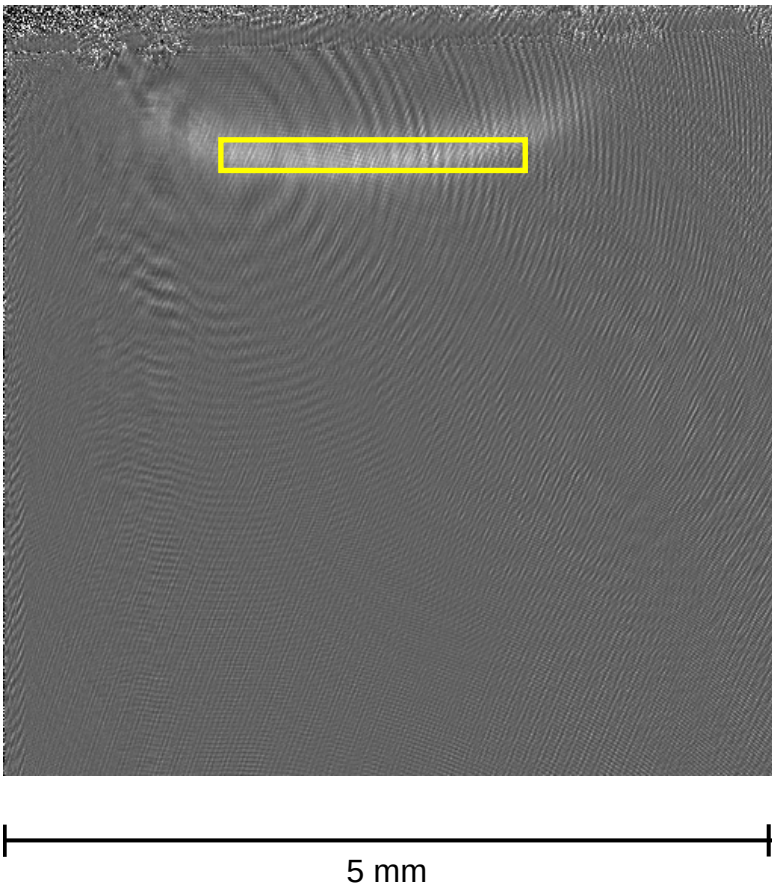

Figure 4.14: Direct in-trap image of the S-trap. By maximizing the population near the trap zero (the region inside the box), the RF frequency sweep can be optimized.

Chapter 5

Conclusions

5.1 Summary

A system suitable for studying interactions between ^{87}Rb Rydberg atoms and metal surfaces has been constructed. Atoms are loaded into a vapor cell mirror MOT and transferred to a macroscopic Ioffe-Pritchard trap, where they will be RF evaporatively cooled and loaded into a magnetic microtrap (atom chip). The design and procedure for the MOT and magnetic trapping follow the outline of Ref. [31]. The magnetic microtrap allows confinement of cold clouds at a controllable distance away from the surface of the chip. Rydberg atom spectroscopy can be performed on atoms at various distances away from the chip and the effects of atom-surface interactions can be studied. The chip currently in the chamber is not suitable for Rydberg atom studies, but will allow the procedures for cooling and loading the ground-state atoms to be developed. A suitable chip, with a flat electrostatic shield above the trapping wires, has been fabricated [37].

Some functionality of the apparatus has been demonstrated. Approximately 1.5×10^7 atoms were loaded into the MOT. After optical molasses cooling and optical pumping to the $|F = 2, m_F = 2>$ hyperfine ground state, approximately 6×10^6

atoms were confined in the macroscopic Ioffe-Pritchard trap. The temperature of the cloud in the trap was 42 ± 5 μK, and the $1/e$ lifetime was 1–1.5 s.

Most of the losses from the Ioffe-Pritchard trap are due to collisions with background gas in the chamber. The loss rate is undesirably high (although experiments in this environment will be possible). Lowering the background pressure without reducing the number of trapped atoms should be possible with some simple changes in the operating procedure, such as pulsing the operation of the rubidium dispensers and running the titanium sublimation pump more frequently. Forced RF evaporation has been used to measure the magnetic field at the trap minimum but RF evaporative cooling has not yet been demonstrated.

5.2 Future Work

Following successful implementation of RF evaporative cooling, the cloud will be transferred to the chip. Some preliminary Rydberg state spectroscopy will be performed on atoms trapped near Chip 1, which is currently in the chamber. After this is done, Chip 1 will be removed and replaced with Chip 2, which has an electrostatic shield over the wires and is much more suitable. While Rydberg state spectroscopy near Chip 1 is not expected to give any useful atomic physics results, comparisons to results obtained with Chip 2 are expected to demonstrate the necessity of the electrostatic shield.

Initial Rydberg spectroscopy experiments will focus on the patch potentials near the chip. These will be characterized by observing the broadening of transitions due to the Stark shift. If the patch potentials are sufficiently small, observation of the Lennard-Jones potential will also be attempted.

5.3 Recommendations for Future Experiments

The construction of any experimental apparatus is an educational experience, and some lessons are inevitably learned the hard way. While this setup should work quite nicely, there are a few things that could be improved in future implementations of this design.

The background pressure in future chambers should be reduced to increase the magnetic trap lifetime. Ideally, the background pressure during magnetic trapping should be less than 10^{-9} Torr during operation, or at least an order of magnitude lower than in the current setup. A two-MOT design, in which the mirror MOT is loaded from a low-velocity intense source [36], would be superior. A pyramidal MOT for this purpose is currently being developed by another student in the group [43]. Future chambers should incorporate an LVIS, or at least be designed to allow for easy addition of an LVIS at a later time. The pressure can be lowered further by increasing the pumping speed with larger pumps and better conductance.

The use of a high-temperature bakeout ($> 300°$C would be required) to reduce outgassing of the chamber does not seem practical. The polyimide planarizing dielectric currently used in the fabrication of Chip 2 [37] and the epoxy used to fasten the chip to the U- and S-wires would not survive a high temperature bakeout, so substantial changes to the chip fabrication and mounting would be involved. The ion gauge and RGA have both been useful diagnostic tools and should be retained, despite the advice to the contrary found in Ref. [28].

Simpler and more flexible control systems could be built in future systems by using FPGA-based digital I/O devices. Windows-based computers running LabVIEW can only control events to timing resolutions in the ms range, so hardware-triggered devices should be used wherever possible. As the present control system works quite well, this is not a major priority for upgrade in our setup.

Bibliography

[1] T. F. Gallagher, *Rydberg Atoms*. Cambridge: Cambridge University Press, 1994.

[2] J. E. Lennard-Jones, "Processes of adsorption and diffusion on solid surfaces," *Trans. Faraday Soc.*, vol. 28, pp. 333–359, 1932.

[3] V. Sandoghdar, C. I. Sukenik, E. A. Hinds, and S. Haroche, "Direct measurement of the van der Waals interaction between an atom and its images in a micron-sized cavity," *Phys. Rev. Lett.*, vol. 68, pp. 3432–3435, Jun 1992.

[4] H. B. G. Casimir and D. Polder, "The influence of retardation on the London-van der Waals forces," *Phys. Rev.*, vol. 73, pp. 360–372, Feb 1948.

[5] E. A. Hinds, "Perturbative cavity quantum electrodynamics," in *Cavity Quantum Electrodynamics (Advances in Atomic, Molecular, and Optical Physics)* (P. R. Berman, ed.), Academic Press, 1994.

[6] C. Fabre, M. Gross, J. Raimond, and S. Haroche, "Measuring atomic dimensions by transmission of Rydberg atoms through micrometre size slits," *J. Phys. B: At. Mol. Opt. Phys*, vol. 16, p. L671, 1983.

[7] D. F. Gray, Z. Zheng, K. A. Smith, and F. B. Dunning, "Ionization of K(nd) Rydberg-state atoms at a surface," *Phys. Rev. A*, vol. 38, pp. 1601–1603, Aug 1988.

[8] S. B. Hill, C. B. Haich, Z. Zhou, P. Nordlander, and F. B. Dunning, "Ionization of xenon Rydberg atoms at a metal surface," *Phys. Rev. Lett.*, vol. 85, pp. 5444–5447, Dec 2000.

[9] F. Dunning, H. Dunham, C. Oubre, and P. Nordlander, "Behavior of Rydberg atoms at surfaces: energy level shifts and ionization," *Nucl. Instr. and Meth. B*, vol. 203, p. 69, 2003.

[10] F. Dunning, S. Wethekam, H. Dunham, and J. Lancaster, "Charge transfer rates for xenon Rydberg atoms at metal and semiconductor surfaces," *Nucl. Instr. and Meth. B*, vol. 258, p. 61, 2007.

[11] C. A. Kocher and C. R. Taylor, "High-Rydberg atoms as probes of surface electric fields and sub-monolayer absorption," *Phys. Lett. A*, vol. 124, pp. 68–72, 1987.

[12] Q. A. Turchette, D. Kielpinski, B. E. King, D. Leibfried, D. M. Meekhof, C. J. Myatt, M. A. Rowe, C. A. Sackett, C. S. Wood, W. M. Itano, C. Monroe, and D. J. Wineland, "Heating of trapped ions from the quantum ground state," *Phys. Rev. A*, vol. 61, p. 063418, May 2000.

[13] L. Deslauriers, S. Olmschenk, D. Stick, W. K. Hensinger, J. Sterk, and C. Monroe, "Scaling and suppression of anomalous heating in ion traps," *Phys. Rev. Lett.*, vol. 97, no. 10, p. 103007, 2006.

[14] J. M. McGuirk, D. M. Harber, J. M. Obrecht, and E. A. Cornell, "Alkali-metal adsorbate polarization on conducting and insulating surfaces probed with Bose-Einstein condensates," *Phys. Rev. A*, vol. 69, no. 6, p. 062905, 2004.

[15] D. M. Harber, J. M. Obrecht, J. M. McGuirk, and E. A. Cornell, "Measurement of the Casimir-Polder force through center-of-mass oscillations of a Bose-Einstein condensate," *Phys. Rev. A*, vol. 72, no. 3, p. 033610, 2005.

[16] Y. Lin, I. Teper, C. Chin, and V. Vuletić, "Impact of the Casimir-Polder potential and Johnson noise on Bose-Einstein condensate stability near surfaces," *Phys. Rev. Lett.*, vol. 92, no. 5, p. 050404, 2004.

[17] J. Reichel, W. Hänsel, and T. Hänsch, "Atomic micromanipulation with magnetic surface traps," *Phys. Rev. Lett.*, vol. 83, p. 3398, 1999.

[18] R. Folman, P. Krüger, D. Cassettari, B. Hessmo, T. Maier, and J. Schmiedmayer, "Controlling cold atoms using nanofabricated surfaces: Atom chips," *Phys. Rev. Lett.*, vol. 84, pp. 4749–4752, May 2000.

[19] C. Monroe, W. Swann, H. Robinson, and C. Wieman, "Very cold trapped atoms in a vapor cell," *Phys. Rev. Lett.*, vol. 65, pp. 1571–1574, Sep 1990.

[20] W. Ketterle and N. J. V. Druten, "Evaporative cooling of trapped atoms," *Adv. At. Mol. Opt. Phys.*, vol. 37, pp. 181–236, 1996.

[21] R. Folman, P. Krüger, J. Schmiedmayer, J. Denschlag, and C. Henkel, "Microscopic atom optics: From wires to an atom chip," *Adv. At. Mol. Opt. Phys.*, vol. 48, p. 263, 2002.

[22] J. Fortagh and C. Zimmermann, "Magnetic microtraps for ultracold atoms," *Rev. Mod. Phys.*, vol. 79, no. 1, p. 235, 2007.

[23] G. K. Woodgate, *Elementary atomic structure*. Oxford University Press, 2nd edition ed., 1980.

[24] D. E. Pritchard, "Cooling neutral atoms in a magnetic trap for precision spectroscopy," *Phys. Rev. Lett.*, vol. 51, no. 15, 1983.

[25] H. Metcalf and P. van der Straten, *Laser cooling and trapping*. Springer-Verlag, 1999.

[26] D. A. Steck, *Rubidium 87 D line data.* Los Alamos National Laboratory, 2003. http://george.ph.utexas.edu/ dsteck/alkalidata/rubidium87numbers.pdf.

[27] W. Hänsel, P. Hommelhoff, T. W. Hänsch, and J. Reichel, "Bose-Einstein condensation on a microelectronic chip," *Nature*, vol. 413, pp. 498–501, 2001.

[28] H. J. Lewandowski, D. M. Harber, D. L. Whitaker, and E. A. Cornell, "Simplified system for creating a Bose-Einstein condensate," *J. Low Temp. Phys.*, vol. 132, no. 5/6, 2003.

[29] B. Lu and W. A. van Wijngaarden, "Bose-Einstein condensation in a QUIC trap," *Can. J. Phys.*, vol. 82, pp. 81–102, 2004.

[30] P. Bohlouli-Zanjani, "High resolution microwave spectroscopy of ultra cold Rydberg atoms as a probe of electric and magnetic fields," Master's thesis, University of Waterloo, 2003.

[31] S. Wildermuth, P. Krüger, C. Becker, M. Brajdic, S. Haupt, A. Kasper, R. Folman, and J. Schmiedmayer, "Optimized magneto-optical trap for experiments with ultracold atoms near surfaces," *Phys. Rev. A*, vol. 69, p. 030901, 2004.

[32] H. Ott, J. Fortagh, G. Schlotterbeck, A. Grossmann, and C. Zimmermann, "Bose-Einstein condensation in a surface microtrap," *Phys. Rev. Lett.*, vol. 87, p. 230401, Nov 2001.

[33] T. L. Gustavson, A. P. Chikkatur, A. E. Leanhardt, A. Görlitz, S. Gupta, D. E. Pritchard, and W. Ketterle, "Transport of Bose-Einstein condensates with optical tweezers," *Phys. Rev. Lett.*, vol. 88, p. 020401, Dec 2001.

[34] Duniway Stockroom Corp., 1305 Space Park Way Mountain View, CA 94043, *Ion gauge gas correction factors.* http://www.duniway.com/images/pdf/pg/ion-gauge-gas-correction-factors.pdf.

[35] B. P. Anderson and M. A. Kasevich, "Loading a vapor-cell magneto-optic trap using light-induced atom desorption," *Phys. Rev. A*, vol. 63, p. 023404, Jan 2001.

[36] Z. T. Lu, K. L. Corwin, M. J. Renn, M. H. Anderson, E. A. Cornell, and C. E. Wieman, "Low-velocity intense source of atoms from a magneto-optical trap," *Phys. Rev. Lett.*, vol. 77, pp. 3331–3334, Oct 1996.

[37] O. Cherry, "Fabrication of an atom chip for Rydberg atom-metal surface interaction studies," Master's thesis, University of Waterloo, 2007.

[38] S. Groth, P. Krüger, S. Wildermuth, R. Folman, T. Fernholz, and J. Schmiedmayer, "Atom chips: Fabrication and thermal properties," *Appl. Phys. Lett.*, vol. 85, p. 2980, 2004.

[39] T. Schumm, J. Estève, C. Figl, J.-B. Trebbia, C. Aussibal, H. Nguyen, D. Mailly, I. Bouchoule, C. Westbrook, and A. Aspect, "Atom chips in the real world: The effects of wire corrugation," *Eur. Phys. J. D*, vol. 32, p. 171, 2005.

[40] C. P. Pearman, C. S. Adams, S. G. Cox, P. F. Griffin, D. A. Smith, and I. G. Hughes, "Polarization spectroscopy of a closed atomic transition: Applications to laser frequency locking," *J. Phys. B: At. Mol. Opt. Phys*, vol. 35, pp. 5141–5151, 2002.

[41] U. Schünemann, H. Engler, R. Grimm, M. Weidemüller, and M. Zielonkowski, "Simple scheme for tunable frequency offset locking of two lasers," *Rev. Sci. Instrum.*, vol. 70, pp. 242–243, January 1999.

[42] S. Chu, L. Hollberg, J. E. Bjorkholm, A. Cable, and A. Ashkin, "Three-dimensional viscous confinement and cooling of atoms by resonance radiation pressure," *Phys. Rev. A*, vol. 55, pp. 48–51, Jul 1985.

[43] B. Lebert. private communication.